UCRL-11243

University of California

Ernest O. Lawrence Radiation Laboratory

TWO-WEEK LOAN COPY

This is a Library Circulating Copy which may be borrowed for two weeks. For a personal retention copy, call Tech. Info. Division, Ext. 5545

NEUTRONS FROM NEGATIVE MU-MESON CAPTURE

Berkeley, California

DISCLAIMER

This document was prepared as an account of work sponsored by the United States Government. While this document is believed to contain correct information, neither the United States Government nor any agency thereof, nor the Regents of the University of California, nor any of their employees, makes any warranty, express or implied, or assumes any legal responsibility for the accuracy, completeness, or usefulness of any information, apparatus, product, or process disclosed, or represents that its use would not infringe privately owned rights. Reference herein to any specific commercial product, process, or service by its trade name, trademark, manufacturer, or otherwise, does not necessarily constitute or imply its endorsement, recommendation, or favoring by the United States Government or any agency thereof, or the Regents of the University of California. The views and opinions of authors expressed herein do not necessarily state or reflect those of the United States Government or any agency thereof or the Regents of the University of California.

Research and Development

UCRL-11243

UNIVERSITY OF CALIFORNIA
Lawrence Radiation Laboratory
Berkeley, California

AEC Contract No. W-7405-eng-48

NEUTRONS FROM NEGATIVE MU-MESON CAPTURE

Burns Macdonald

(Ph. D. Thesis)

June 29, 1964

NEUTRONS FROM NEGATIVE MU-MESON CAPTURE

Contents

Abstract v

I. Introduction 1

II. Theory

A. Nuclear Excitation 4

1. Fermi Gas Momentum Distribution 6

2. Gaussian Momentum Distribution 8

3. Shell Model 8

B. Neutron Emission 9

1. Neutron Multiplicity Distribution 9

2. Direct-Emission Corrections 13

C. Nucleon Effective Mass 13

III. Experimental Procedure

A. Beam 17

B. Scintillator Tank 23

1. Physical Description 23

2. Method of Neutron Detection 25

3. Calibration of Efficiency 25

C. Operation, Telescope, and Electronics 28

IV. Data Analysis 32

V. Results and Discussion

A. Experimental Results 38

B. Comparison with Other Experiments 38

C. Comparison of Experiment with Theory 38

VI. Conclusions 66

Acknowledgments 67

Appendix 68

References 71

NEUTRONS FROM NEGATIVE MU-MESON CAPTURE

Burns Macdonald

Lawrence Radiation Laboratory
University of California
Berkeley, California

June 29, 1964

ABSTRACT

Average neutron emission and neutron multiplicity distributions from μ^--meson capture in Al, Si, Ca, Fe, Ag, I, Au, and Pb were measured. A high-efficiency cadmium-loaded liquid scintillator tank was used having an efficiency of 54.5% for detecting neutrons from fission. Fermi gas and Gaussian nuclear models are used to fit the experimental results. A reduced nucleon effective mass is employed to give the observed average neutron multiplicity, and values are obtained as a function of the width of the nucleon momentum distribution assumed. Use of the Gaussian momentum distribution obtained in experiments on quasi-elastic scattering gives effective masses ranging from $\approx 0.7\ M_p$ in the lighter nuclei to $\approx 0.45\ M_p$ in the heavier nuclei. An excited Fermi gas distribution gives larger effective masses for the lighter nuclei and smaller effective masses for the heavier nuclei than does the Gaussian model. With either of these models the distributions of neutron multiplicities cannot be explained without allowing for direct neutron emission and clustering on the nuclear surface.

For Ca^{40} a shell-model calculation with a simple harmonic oscillator potential gave good agreement with the observed average neutron multiplicity.

For both the Fermi gas and Gaussian models, the average nuclear excitation energy varies linearly with average neutron multiplicity and is relatively insensitive to the model parameters. When the

average neutrino momentum is expressed in units of the muon mass reduced by its K-shell binding energy the result (with the exception of doubly magic calcium) is constant, 0.82 ± 0.01, over the wide range of atomic numbers covered in the experiment.

I. INTRODUCTION

The negative μ meson has been used by many investigators as a tool for inquiry into specifically nuclear and atomic properties. For example, μ-meson scattering as well as the x-ray spectra of μ-mesonic atoms is sensitive to the size and structure of the nucleus.[1] Experiments on μ^- capture in compounds have found the relative atomic capture probabilities of particles near the end of their range.[2] Mu-meson-induced fission has been studied and the relative probability of radiationless-transition fissions determined.[3] Nuclear temperatures have been ascertained from nuclei excited by μ^- capture.[4]

The experiment presented here continues an investigation by Kaplan, Moyer, and Pyle into nuclear momentum distributions and nucleon effective masses by measurements of the number of neutrons boiled off.[5]

Negative muons entering solid matter are slowed down, are captured by an atom, and cascade down to the mesic-atom K shell in a time very short compared with the μ's decay lifetime.[6]

A muon in the K shell spends at least a part of its time within the nucleus. Thus there is a large probability, in not too light nuclei, of the μ-meson's being captured by the proton according to the weak-interaction process,

$$\mu^- + p \rightarrow n + \nu. \tag{1}$$

In competition with this reaction is the muon's decay, $\mu^- \rightarrow e^- + \nu + \bar{\nu}$. (In the elements studied here, the fraction that decays ran from $\approx 3\%$ in lead to $\approx 40\%$ in aluminum.)

In the capture process the neutrino takes off most of the energy. With a proton at rest, the neutron recoils with about 5 MeV. The energy of recoil in heavy nuclei is usually absorbed by the nucleus; this leaves

the nucleus in an excited state. Since the proton in the nucleus typically is moving at the time of capture, the recoil energy of the neutron in the rest system of the nucleus is different from 5 MeV. The neutron, and hence the nucleus, will have a distribution of energies, I(Q), which depends on the momentum distribution of the capturing proton.

Measurements of the average number of neutrons emitted[5, 7] indicate nuclear excitations of 10 to 15 MeV. Nuclei at these excitations are known to decay primarily by neutron emission when energetically possible. Proton emission is small compared with neutron emission because of the effect of the Coulomb barrier at these moderate excitations ($\approx$ 0.025 protons per capture in silver and bromine[8]). Photons are given off only when the excitation is below the threshold for particle emission. Thus a knowledge of the numbers of neutrons given out following μ-meson capture yields information about the nuclear excitation distribution and thus about the proton momentum distribution.

The above picture of nuclear excitations from μ-meson capture was first suggested by Rosenbluth[9] and Tiomno and Wheeler[10] in calculations of the nuclear excitation distribution with a degenerate Fermi-gas momentum distribution. Neutron multiplicities were later found to be greater than expected on the basis of this model.[11]

Lang applied the idea of nucleon effective mass in order to explain these higher multiplicities.[12] The average potential acting on a nucleon inside a nucleus is known from optical model analyses to be momentum dependent.[13,14] The effect of this momentum dependence is to replace the unbound nucleon mass, M, by a smaller effective mass, M^*, in the equation connecting the nucleon's energy and its momentum,

$$E = p^2/2M^* . \qquad (2)$$

Calculations on the basis of several nuclear models predict nucleon effective masses of about 0.5 M.[15-17]

The effective mass can be adjusted to give the same value of average neutron emission for different choices of the nucleon momentum distribution or the nuclear model. However, the distribution of neutron multiplicities is generally different for the various distributions or models.

The first accurate measurement of the distribution of multiplicities was made by Kaplan, Moyer, and Pyle for silver and lead; they used cosmic-ray μ mesons and a large cadmium-loaded liquid scintillator tank as a high-efficiency neutron detector.[5] There was considerable advantage to be gained, in terms of counting rate and purity of beam, by using μ's from the 184-inch cyclotron, and this experiment was carried out, with the same neutron detector, for eight targets ranging from aluminum to lead.

II. THEORY

In the following, the nuclear excitation distribution is derived with the assumption that the μ meson interacts according to (1) with a single proton, transforming it into a neutron with emission of a neutrino. The rest of the nucleus is assumed to take no part in the reaction and the momentum of the interacting particles is conserved.

The form of the excitation distribution, I(Q), is given upon the assumption of a Fermi gas momentum distribution for the capturing protons, following Kaplan et al.[5] I(Q) for a Gaussian momentum distribution is also given, following Singer,[18] since the Gaussian distribution has been shown to give good fits for "quasi-elastic" scattering experiments in lighter nuclei[19-21] and for π-meson production near threshold.[22] A spectrum of nuclear excitations by μ^- capture, on the basis of a shell-model calculation for Ca^{40}, is also presented.[23]

The nuclear excitation is then related to the neutron multiplicity distribution by compound-nucleus evaporation theory.[5] Direct emission and nuclear surface effect corrections to the evaporation model are given.[18,24]

The idea of a nucleon effective mass is discussed and applied to the calculations of neutron emission in order to produce agreement of the calculated average neutron multiplicities with those observed. For comparison, effective masses are also derived from nuclear level densities.[25]

A. Nuclear Excitation

A μ^- meson, in a μ-mesonic K shell, is captured by a nucleus (Z, A) which is considered to consist of the capturing proton, moving with a certain momentum dis tribution, plus a "core" nucleus (Z-1, A-1) which does not take part in Reaction (1). The momentum of muons compared with the nucleon momenta is neglected. Energy conservation

gives

$$\mu^2 - B_\mu + M(Z, A)c^2 = kc + M(Z-1, A)c^2 + Q. \qquad (2)$$

The rest energy of the muon is μc^2, and B_μ is its K-shell binding energy; $M(Z, A)$ and $M(Z-1, A)$ are the masses of the target and product nuclei, and kc is the energy of the neutrino; Q is the excitation energy of the product nucleus, $(Z-1, A)$, if its small recoil energy is neglected. Defining E_0 as the maximum energy available to the product system, we get

$$E_0 = kc + Q, \qquad (3)$$

where $$E_0 = \mu c^2 - B_\mu + M(Z, A) - M(Z-1, A).$$

The momentum conservation equation is the one obtained for Reaction (1), since the "core" nucleus is assumed to take only a spectator role:

$$\underset{\sim}{p} = \underset{\sim}{q} + \underset{\sim}{k}, \qquad (4)$$

where $\underset{\sim}{p}$, $\underset{\sim}{q}$, and $\underset{\sim}{k}$ are the momenta of the capturing proton, the resulting neutron, and the emitted neutrino respectively.

The μ-capture probability is given in first order by perturbation theory,

$$\omega = \frac{2\pi}{\hbar} \sum_f |H_{if}|^2 \rho_f.$$

Since we are interested in the nuclear excitation distribution and not in the details of the weak interaction, we assume a simple form of the interaction Hamiltonian,[18]

$$H = G\, \tau_N\, \tau_L\, \delta(\underset{\sim}{r}_N - \underset{\sim}{r}_L) + C.C.,$$

where τ_N converts a proton into a neutron, τ_L converts an electron into a neutrino, and G is the weak interaction coupling constant. The neutrino wave function is a plane wave. The muon wave function is assumed to be constant over the nucleus. The nuclear wave function is taken to be the products of individual independent nucleon wave functions, the final nuclear wave function differing from the initial in only one nucleon. The interaction between nucleons is approximated by assuming a reduced "effective mass" for the nucleons.

Summing over the final spin states of neutron and neutrino and averaging over initial spins for the capturing proton and the muon gives

$$\omega = K' \int d^3\underset{\sim}{k}\ d^3\underset{\sim}{p}\ d^3\underset{\sim}{q}\ f(\underset{\sim}{p})[1 - g(\underset{\sim}{q})]\ \delta(\underset{\sim}{k} + \underset{\sim}{q} - \underset{\sim}{p})\ \delta(E_0 - kc - Q). \qquad (5)$$

Here K' is a constant; $f(\underset{\sim}{p})$ and $g(\underset{\sim}{q})$ are the probabilities per unit volume of momentum space of finding a proton of momentum $\underset{\sim}{p}$ and a neutron of momentum $\underset{\sim}{q}$; the factor, $[1 - g(q)]$, contributed by the Pauli exclusion principle, ensures that the neutron is created only in states unoccupied by neutrons; f and g are known if the ground-state nuclear wave function is known. We assume a Fermi gas and a Gaussian model for these distributions.

In order to express the transition probability in the form

$$\omega \propto \int I(Q)\, dQ, \qquad (6)$$

where I(Q) is interpreted as the excitation distribution of the nucleus, the nuclear excitation, Q, must be related to the momenta.

1. Fermi Gas Momentum Distribution

The excitation of the product nucleus is taken to be the difference between the total energies of the neutron and the capturing proton:

$$Q = E_n - E_p = (T_n + V_n) - (T_p + V_p).$$

The completely degenerate Fermi gas model gives, for the difference between the proton and neutron well depths, $(V_p - V_n) = (q_0^2 - p_0^2)/2M^*$,

where M^* is the nucleon effective mass, assumed equal for proton and neutron. Therefore

$$Q = \frac{(q^2 - p^2)}{2M^*} - \frac{(q_0^{\,2} - p_0^{\,2})}{2M^*} . \tag{7}$$

The momentum distribution functions for a degenerate Fermi gas are given by

$$f(\underset{\sim}{p}) = 1/\left\{1 + \exp[(p^2 - p_0^{\,2})/2M\,\theta_f]\right\},$$

$$g(\underset{\sim}{q}) = 1/\left\{1 + \exp[(q^2 - q_0^{\,2})/2M\,\theta_f]\right\},$$

where θ_f is the Fermi temperature in energy units (MeV).

Substitution of Eqs. (7) and (4) into (3) gives a relationship between $\underset{\sim}{k}$ and $\underset{\sim}{p}$:

$$E_0 = kc - \frac{(q_0^{\,2} - p_0^{\,2})}{2M^*} = \frac{(k^2 - 2\underset{\sim}{k} \cdot \underset{\sim}{p})}{2M^*} .$$

Use of this in the integration of Eq. (5) over all variables except k yields

$$\omega \propto \int kdk \left\{1 - \exp[(kc - E_0)/2\theta_f]\right\}^{-1} \ln \left\{\frac{1 + \exp[(a + E_0 - kc)/2\theta_f]}{1 + \exp[(a - E_0 + kc)/2\theta_f]}\right\},$$

where $$a = \frac{(q_0^{\,2} + p_0^{\,2})}{2M^*} - \frac{k^2}{4M^*} - \frac{M^*[E_0 - kc - (q_0^{\,2} - p_0^{\,2})/2M^*]^2}{k^2} .$$

The change of variable from k to Q ($kc = E_0 - Q$) gives an equation of the form of Eq. (6), where

$$I(Q) = \frac{2\theta_f K(E_0 - Q)}{1 - \exp(-Q/\theta_f)} \ln \left\{\frac{1 + \exp[(a + Q)/2\theta_f)]}{1 + \exp[(a - Q)/2\theta_f)]}\right\} . \tag{8}$$

(The normalization constant K is determined by $\int I(Q)dQ = 1.$)

For a completely degenerate Fermi gas ($\theta_f = 0$),

$$I(Q) = 2K(E_0 - Q)Q \qquad \text{for} \quad (a - Q) \geq 0,$$
$$= K(E_0 - Q)(a + Q) \qquad \text{for} \quad (a - Q) \leq 0.$$

2. Gaussian Momentum Distribution

If a Gaussian momentum distribution of the nucleons is assumed, then

$$f(\underset{\sim}{p}) = \exp(-p^2/a^2),$$
$$g(\underset{\sim}{q}) = \exp(-q^2/a^2).$$

The nuclear excitation distribution derived from Eq. (5) then becomes

$$I(Q) = K'(E_0 - Q)\left\{\exp[-f_1(Q)] - 1/2 \exp[-2f_2(Q)]\right\}, \qquad (9)$$

where
$$f_1(Q) = \frac{1}{a^2}\left\{\frac{(E_0 - Q)^2}{4} - MQ + \frac{M^2Q^2}{(E_0 - Q)^2}\right\},$$
$$f_2(Q) = \frac{1}{a^2}\left\{\frac{(E_0 - Q)^2}{4} + \frac{M^2Q^2}{(E_0 - Q)^2}\right\},$$

and K' is a normalization constant.

3. Shell Model

It is of interest to calculate the nuclear excitation distribution from a shell model. $I(Q)$ then becomes a discrete spectrum of energies. Luyten, Rood, and Tolhoek have found $I(Q)$ for Ca^{40} from a simple harmonic oscillator shell model.[26] This simple model is not suitable for evaluating neutron emission, since it predicts nuclear excitations of multiples of 10.1 MeV only. We have extended their calculation by splitting the simple harmonic oscillator energy levels with terms proportional to $\underset{\sim}{\ell} \cdot \underset{\sim}{s}$ and to ℓ^2. The Hamiltonian becomes

$$H = \hbar\omega_0 - 2\hbar\omega_0 \chi\, \underset{\sim}{\ell} \cdot \underset{\sim}{s} - \hbar\omega_0 \chi \mu \ell^2$$

(the ℓ^2 term gives a correction to the harmonic oscillator potential for high ℓ values, which serves to depress high angular momentum states). The values of the constants $\hbar\omega_0$, χ, and μ are taken from Nilsson:[27]

$$\hbar\omega_0 = 41\ A^{-1/3}(\text{MeV}) = 12.0\ \text{MeV}.$$

Results are given in Fig. 25.

B. Neutron Emission

The neutron produced in the μ capture is assumed quickly to share its kinetic energy with the other nucleons to produce an excited compound nucleus. (Direct emission of the neutron is discussed later.) Charged-particle emission is negligible for the moderate excitations obtained here, and the nucleus boils off neutrons with the energy distribution[28]

$$N(\epsilon) \propto \epsilon \exp(-\epsilon/\theta),$$

where ϵ is the neutron kinetic energy, and the nuclear temperature, θ, is a constant which depends on the excitation. Since the neutron emission is relatively insensitive to the value of the nuclear temperature, we assumed θ to be constant during the course of the de-excitation of the nucleus. The value chosen for all targets used was $\theta = 0.75$ MeV.[29]

Neutron emission continues until the excitation is less than the neutron separation energy. Only then does gamma emission become important, and the nucleus decays to its ground state.

1. The Neutron Multiplicity Distribution

Let B_ν be the sum of the first ν neutron binding energies. At least ν neutrons will be emitted if the nuclear excitation is greater than B_ν plus the sum of the kinetic energies of the first $(\nu - 1)$ neutrons, that is, if $(Q - B_\nu) \geq \epsilon_1 + \epsilon_2 + \cdots \epsilon_{\nu-1}$. The probability that at least ν

neutrons are emitted from a nucleus with excitation Q is

$$N_\nu = K'' \int_0^{Q-B_\nu} \epsilon_{\nu-1} \exp(-\epsilon_{\nu-1}/\theta)\, d\epsilon_{\nu-1}$$

$$\times \int_0^{Q-B_\nu-\epsilon_{\nu-1}} \epsilon_{\nu-2} \exp(-\epsilon_{\nu-2}/\theta) d\,\epsilon_{\nu-2} \cdots$$

$$\times \int_0^{Q-B_\nu-\epsilon_{\nu-1}-\cdots-\epsilon_2} \epsilon_1 \exp(-\epsilon_1/\theta) d\,\epsilon_1 \; .$$

Integrating and determining the normalization from $N_\nu \to 1$ for large $(Q-B_\nu)$ yields

$$N_\nu = 1 - \exp\left[-(Q-B_\nu)/\theta\right] \sum_{n=0}^{2\nu-3} \left[\frac{Q-B_\nu}{\theta}\right]^n \frac{1}{n!} \; .$$

The probability for emission of just ν neutrons by a nucleus with a distribution of excitations $I(Q)$ is

$$P_\nu = \frac{\int_{B_\nu}^{E_0} N_\nu I(Q) dQ}{\int_0^{E_0} I(Q)\, dQ} - \frac{\int_{B_{\nu+1}}^{E_0} N_{\nu+1}\, I(Q) dQ}{\int_0^{E_0} I(Q)\, dQ} \; ,$$

where $P_0, P_1, P_2, \cdots$ are the probabilities, normalized to one, for emitting 0, 1, 2, ... neutrons.

The integrals were done numerically for the various excitation distributions. The constants used are given in Tables I and II.

Table I. Isotopic abundances, nuclear mass differences, muon binding energies, total muon disappearance rates, and decay rates.

Target	Atomic number	Abundance[a]	Product nucleus	M(Z, A)-M(Z-1, A)[b] (MeV)	B_μ[c] (MeV)	$\lambda \times 10^{-5}$[d] (sec^{-1})	$\lambda_d \times 10^{-5}$[e] (sec^{-1})	λ_d / λ
$_{13}Al$	27	1.000	$_{12}Mg$	3.129	0.463	11.32	4.54	0.401
$_{14}Si$	28	0.922	$_{13}Al$	5.151	0.535	12.06	4.54	0.376
$_{20}Ca$	40	0.970	$_{19}K$	1.833	1.054	29.6	4.54	0.153
$_{26}Fe$	56	0.917	$_{25}Mn$	4.220	1.72	51.0	4.45	0.087
$_{47}Ag$	107	0.514	$_{46}Pd$	0.546	4.76	118.5	4.16	0.0351
$_{47}Ag$	109	0.486	$_{46}Pd$	1.624				
$_{53}I$	127	1.000	$_{52}Te$	1.200	5.80	116.1	4.13	0.0356
$_{79}Au$	197	1.000	$_{78}Pt$	1.26	10.10	145.8	3.8	0.0261
$_{82}Pb$	206	0.236	$_{81}Tl$	2.02	10.66	134.9	3.8	0.0282
$_{82}Pb$	207	0.226	$_{81}Tl$	1.953				
$_{82}Pb$	208	0.523	$_{81}Tl$	5.506				

a. See Ref. 43 b. See Ref. 44 c. See Ref. 45 d. See Ref. 46 e. See Ref. 47

Table II. Neutron separation energies.

Target Nucleus	→	Product Nucleus		Neutron separation energies (MeV)[a]								
$_{13}Al$	→	$_{12}Mg$	A	27	26	25	24	23				
				6.437	11.097	7.331	16.535	13.442				
$_{14}Si$	→	$_{13}Al$	A	28	27	26	25	24				
				7.723	13.069	11.344	17.090	12.9[b]				
$_{20}Ca$	→	$_{19}K$	A	40	39	38	37	36	35	34	33	
				7.798	13.079	12.030	15.154[b]	12.835	17.6[b]	15.8[b]	22.0[b]	
$_{26}Fe$	→	$_{25}Mn$	A	56	55	54	53	52	51	50		
				7.270	10.220	8.940	12.049	10.529	13.47	12.3[b]		
$_{47}Ag$	→	$_{46}Pd$	A	109	108	107	106	105	104	103	102	101
				6.24[c]	9.08[c]	6.39[c]	9.41[c]	7.409[c]	9.80[c]	7.62[c]	10.26[c]	9.01[c]
$_{53}I$	→	$_{52}Te$	A	127	126	125	124	123	122	121	120	
				6.353[c]	9.099[c]	6.577[c]	9.417[c]	6.789[c]	9.9[b]	7.6[b]	10.2[b]	
$_{79}Au$	→	$_{78}Pt$	A	197	196	195	194	193	192	191	190	
				5.86	7.92	6.21	8.55	6.3	7.8[b]	6.4[b]	8.3[b]	
$_{82}Pb$	→	$_{81}Tl$	A	208	207	206	205	204	203	202	201	200
				3.83	6.80	6.56	7.54	6.62	7.88	6.79	8.2[b]	6.5[b]

a. From L. A. König, J. H. E. Mattauch, and A. H. Wapstra, Nucl. Phys. 31, 18 (1962), except as noted.

b. A. G. W. Cameron, A Revised Semi-Empirical Atomic Mass Formula, Chalk River Report CRP-690, 1957 (unpublished.)

c. V. A. Kravtsov, Nucl. Phys. 41, 330 (1963).

The values of P_ν were then averaged over the natural isotopic abundances of the targets (Table I). The values obtained are those expected with a 100% efficient detector. To compare with experimental values of the neutron multiplicities, the P_ν's were converted to the distribution (F_0, F_1, F_2,$\cdots$) expected with a detector of efficiency e(where e = 0.545):

$$F_n = e^n \sum_{\nu=n}^{\infty} P_\nu (1-e)^{\nu-n} \frac{\nu!}{n!(\nu-n)!} . \tag{10}$$

2. Direct-Emission Corrections

The above calculation of the neutron multiplicity distribution has assumed that a compound nucleus is always formed. In a simple calculation, Singer finds that the direct emission of the neutron resulting from μ^- capture is not negligible, even for heavy nuclei.[18] His results for the fraction of time that a single neutron is directly emitted are

Ag, 0.216; I, 0.199; Au, 0.157; Pb 0.153.

In an effort to obtain a higher neutron emission Singer investigates the effects of nucleon clustering on the nuclear surface.[24] For silver, he estimates that 14.4% of the time a μ meson is captured on a pseudo-deuteron cluster on the surface and two neutrons are emitted.

The effect of these corrections on the effective mass is given in Table X.

C. Nucleon Effective Mass

The idea of a nucleon "effective mass" within nuclear matter that is different from the free nucleon mass is a direct consequence of the existence of a nonlocal potential in the nucleus.[30] If the presence of a particle at a point $\underset{\sim}{r}'$ influences the probability of finding another particle at a neighboring point $\underset{\sim}{r}$, then the energy operator is not diagonal in coordinate space and the Schrödinger equation is

$$E\psi(\underset{\sim}{r}) = -\frac{\hbar^2}{2M}\nabla_r^2\psi(\underset{\sim}{r}) + \int d\underset{\sim}{r}'\, V(\underset{\sim}{r}, \underset{\sim}{r}')\,\psi(\underset{\sim}{r}').$$

If we assume the wave function is a plane wave of constant momentum(noninteracting Fermi gas), $\psi = \exp(i\,\underset{\sim}{p}\cdot\underset{\sim}{r}/\hbar)$, the equation becomes

$$E = \frac{p^2}{2M} + \int d\underset{\sim}{r}'\, V(\underset{\sim}{r}, \underset{\sim}{r}')\exp\left[i\underset{\sim}{p}\cdot(\underset{\sim}{r}' - \underset{\sim}{r})/\hbar\right].$$

If $V(\underset{\sim}{r}, \underset{\sim}{r}')$ depends only on the relative coordinate $(\underset{\sim}{r}' - \underset{\sim}{r})$, as is reasonable to suppose, then the integral term does not depend on $\underset{\sim}{r}$, but only on the momentum:

$$E = \frac{p^2}{2M} + V(p),$$

where $V(p)$ is just the Fourier transform of $V(\underset{\sim}{r}'-\underset{\sim}{r})$ (Gomes, Walecka, and Weisskopf, in their independent-pair model, show that, except for close distances within the "healing distance," the wave function is indeed that of noninteracting particles.[31])

Momentum dependence of the nucleon potential is well known from nucleon scattering and optical-model analyses.[13,14,32,33] If the potential is expressed as a power series in p^2 (there are no odd terms if the potential is to be invariant under time inversion), we have $V(p) = V_0 + bp^2$ to first order in p^2. Then

$$E \cong p^2/2M + bp^2 + V_0, \text{ or}$$
$$E = \frac{p^2}{2M^*} + V_0, \tag{11}$$

where
$$\frac{1}{M^*} = \frac{1}{M} + 2b.$$

Thus, the energy dependence of a nucleon moving in a nonlocal potential is the same as for a particle with an effective mass M^* in a constant potential.

A momentum-independent effective mass is a good approximation in accounting for the effect of nonlocal potentials, as shown, for example, by Clementel and Villi.[25] They have calculated the momentum dependence of the potential with a Fermi gas for several choices of the two-body potential, $V(\underset{\sim}{r}' - \underset{\sim}{r})$. Their results show, independent of the exact $V(\underset{\sim}{r}' - \underset{\sim}{r})$ assumed, that $V(p)$ is quite closely quadratic in p for all momenta less than the Fermi momentum, not just those around $p = 0$.

More exactly, the effective mass depends somewhat on momentum. In calculations for extended nuclear matter, Brueckner and Gammel get $M^* = 0.56\,M$ for $p = 0$ and $M^* = 0.66M$ for $p = p_f$, the Fermi momentum.[16] For higher momenta the momentum dependence of the potential becomes small and $M^*(p) \rightarrow M$.

The average value of the effective mass is given by the average of $M^*(p)$ over the momentum distribution of the nucleons. For μ^--meson capture the amount of high momenta is small and one can write

$$M^* = \frac{\int_0^{p_f} M^*(p)\, p^2 dp}{\int_0^{p_f} p^2\, dp} = \frac{\int_0^{p_f} M \cdot (0.56 + 0.10\, p^2/p_f^{\,2}) p^2 dp}{\int_0^{p_f} p^2\, dp} = 0.62\ M.$$

Results for finite nuclei give values of effective mass smaller than that expected for extended nuclear matter. Brueckner, Lockett, and Rotenberg, in calculations for Zr^{90}, Ca^{40}, and O^{16}, get an effective mass for Zr^{90} of 0.39 M.[17] Values of $M^* \approx 0.5\ M$ are indicated by a number of calculations.

With use of an effective mass of 0.55 M very good agreement has been obtained for the total photonuclear absorption cross section and giant γ-ray absorption resonance frequencies for medium and heavy nuclei.[34]

Clementel and Villi have estimated nucleon effective masses from known values of nuclear level spacings.[25] At an excitation Q the level spacing is

$$D_0(Q) = (4\pi)^{1/2} \left(\frac{Q^3}{a^*}\right)^{1/4} \exp[-2(a^* Q)^{1/2}]. \tag{12}$$

The level spacing parameter, a^*, given by Clementel and Villi on the basis of a Fermi gas calculation involves the nucleon effective mass,

$$a^* = \frac{\pi^2 A}{4E_f} \frac{2M^*}{M+M^*}, \tag{13}$$

where E_f is the Fermi energy. Values of M^* from the level spacing data of Hughes et al. are given in Table VI.

III. EXPERIMENTAL PROCEDURE

The number distribution of neutrons emitted by a nucleus which has captured a μ^- meson was measured by using a large cadmium-loaded liquid-scintillator tank which had a high efficiency ($\approx$55%) for detection of a single neutron.

A negative beam of particles was produced within the Berkeley 184-inch 740-MeV cyclotron. Particles of 220 MeV/c momentum were selected by a magnet system (Fig. 1) and detected by a scintillation-counter telescope (Fig. 2). Because of their smaller velocity, π^- mesons are stopped by an amount of CH_2 absorber which allows the muons to pass through and stop in the target. Neutrons from a μ^- capture were detected by the scintillation tank with a 7.8-μsec lifetime. A μ^- stopping in the target triggered an oscilloscope and a 30-μsec gate. The number of neutrons counted during this gate was stored electronically. In addition, the pulses from the scintillator tank were displayed on one sweep of the oscilloscope and the counter-telescope pulses were displayed on another sweep and the display photographed.

A. Beam

Negative particles from the cyclotron's internal target pass through the cyclotron fringing field and a quadrupole magnet to enter the meson wheel, an 8-ft-long iron collimator stopped down to 4×4 in. Coming into the meson cave (Fig. 1), the beam goes through a bending magnet, a 4-ft concrete shielding wall, a second bending magnet, and a second shielding wall.

Since higher neutron multiplicities are affected strongly by pions, considerable attention was directed to reducing to a minimum any pion contamination in the muons stopping in the target.

In order to estimate an upper limit to this contamination, a positive meson beam was put incident on a scintillator target and the $\pi^+-\mu^+$

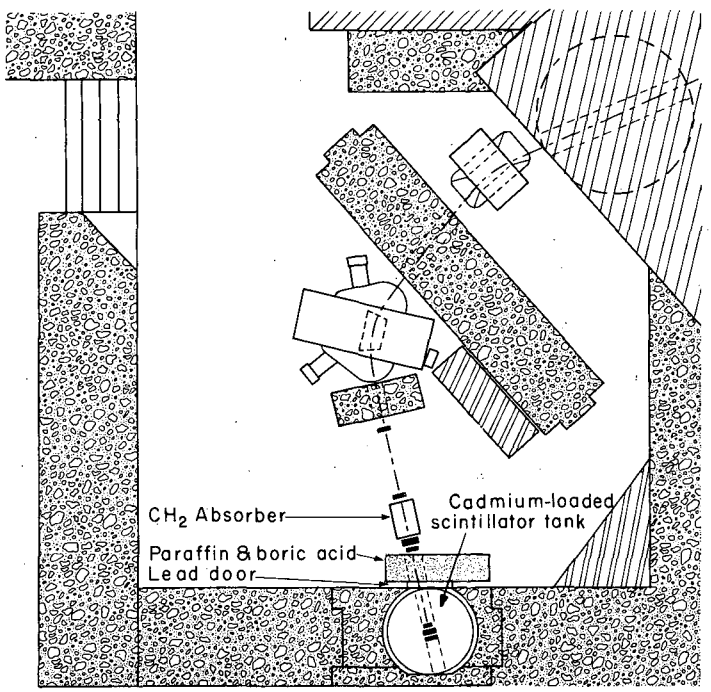

Fig. 1. Experimental setup in the 184-inch cyclotron meson cave.

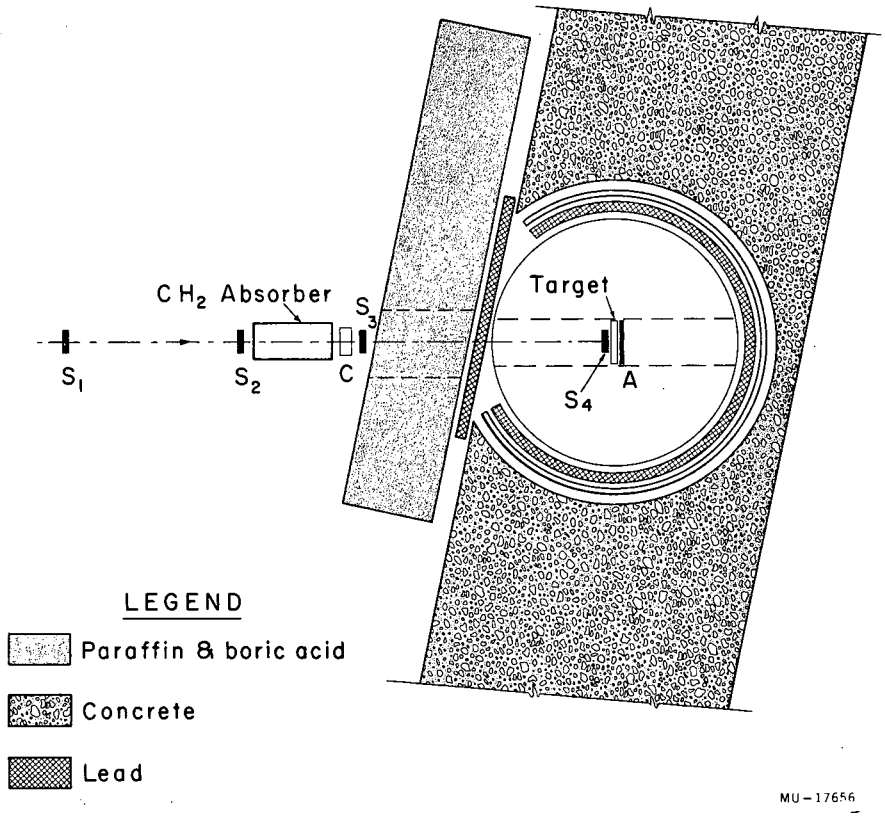

Fig. 2. Experimental arrangement of the counter telescope and cadmium-loaded liquid scintillator tank.

decays counted as a function of CH_2 absorber thickness (Fig. 3). Extrapolation gives 0.0005 as the maximum fraction of particles at the π-range peak which have sufficient range to penetrate 13.5 in. of CH_2 absorber for the momentum definition obtained during the experiment.

The cyclotron was changed over to a negative meson beam and the beam monitor counts were maximized with respect to position of the internal cyclotron target. The ratio of the μ^- peak to π^- peak was about 1/7.

The position of the cyclotron meson target was then changed in order to reduce the relative number of pions in the beam.[35] Its position, although stable in time, influences the beam composition critically. Pi's are produced directly in the cyclotron target. If the target is moved, the counter-telescope no longer looks directly at the meson target but somewhat to one side. Muons entering the telescope then have their source principally in the decay of the pions in a cloud surrounding the meson target.

A differential range curve for the total stoppings in a carbon target inside the scintillation tank (Fig. 4) gives a μ^- peak to π^- peak ratio of 3/1, but with a total μ^- intensity reduced by a factor of 7. This curve, when compared with the $\mu^- - e^-$ decay curve (which has been normalized to the same number of μ^- peak stoppings), shows that the composition of the beam is $\mu/\pi > 5/1$. With this beam composition and by using the π^+ extrapolation datum, the fraction of π's stopping in the target is estimated at less than 0.0001 with 13 in. of CH_2 absorber. The contribution of π's to the average neutron emission is then less than 0.001 neutrons per capture (assuming about five neutrons emitted per π capture). The effect of π's on any given neutron multiplicity is even less than this.

The π contamination was checked experimentally by making measurements for gold for smaller absorber thicknesses. The average neutron emission for gold, corrected only for background, was 1.64 ± 0.05 at 13 in. of CH_2, 1.68 ± 0.07 at 11 in. of CH_2, and 1.95 ± 0.11 at 9 in. of CH_2, showing no significant increase of neutrons for 2 in.

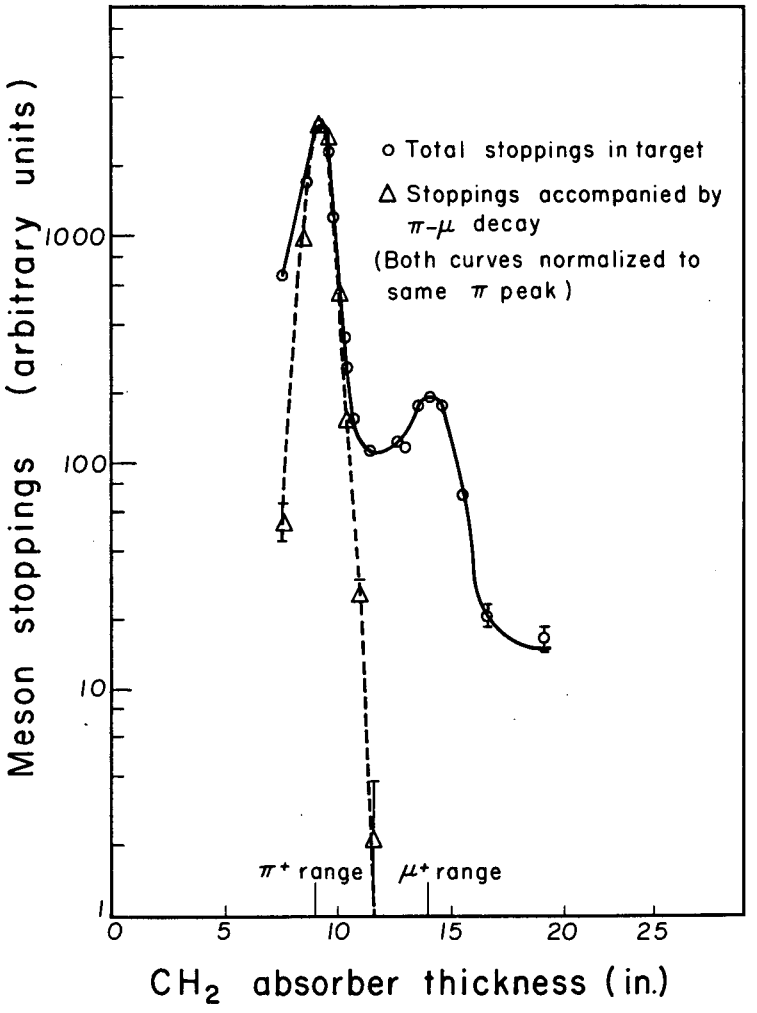

MU-18035

Fig. 3. Positive meson stoppings in the scintillator target.

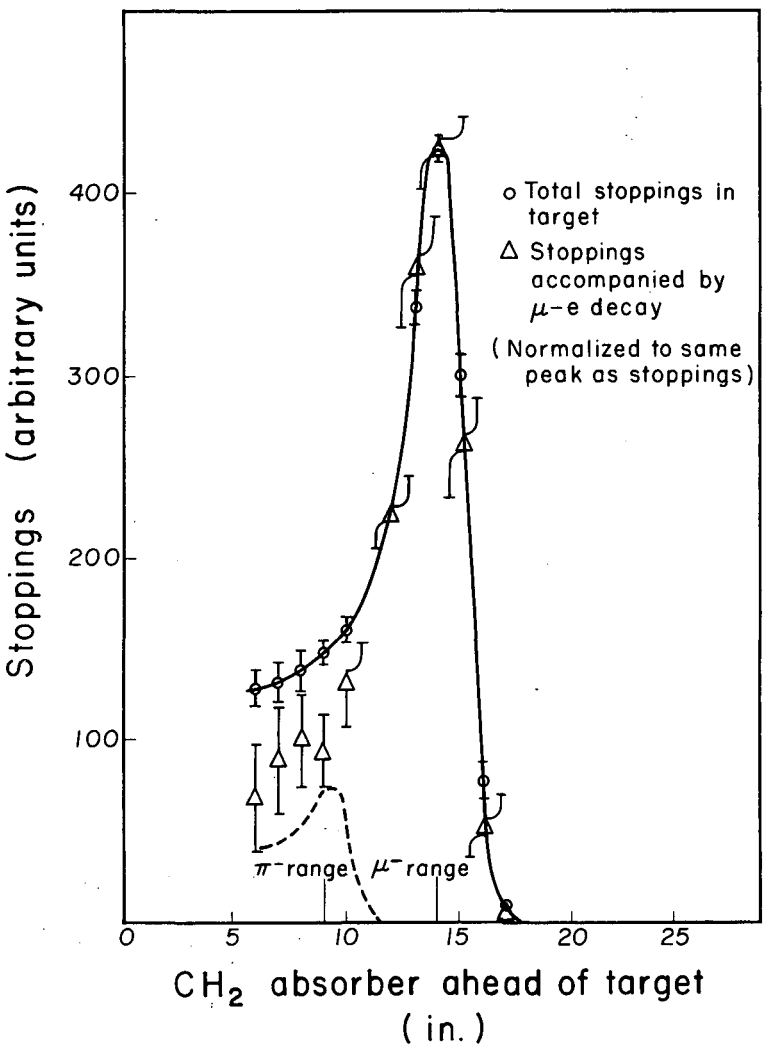

MU-18034

Fig. 4. μ^- stoppings in carbon target.

less absorber than the usual running conditions (13 in.).

Neutron absorption in the target itself is negligible for our targets, as indicated by the work of Kaplan et al.,[5] who got only a small effect for silver and no effect for lead, for targets much thicker than ours.

The effect of possible electrons in the beam was eliminated by requiring that there be no Cerenkov-counter pulse for a μ stopping. That this was effective is shown directly by the data of Fig. 4. For ranges greater than the μ^- range, the total stoppings in the target are very nearly equal to the normalized stoppings of particles identified as μ's by their decay.

B. Scintillator Tank

1. Physical Description

The neutron detector is a tank 30 in. long and 30 in. in diam with 1/4-in. steel walls.[36] The interior has been sprayed with a protective coating of molten aluminum and then with a mixture of aluminum oxide, abrasive powder, water glass, and water to give a final highly reflective surface. The tank was filled with a scintillator solution of toluene mixed with 29.5 lb of cadmium propionate dissolved in 48 lb of methyl alcohol, with p-terphenyl as a scintillator and a spectrum shifter, POPOP.

The curved surface of the tank has 88 glass windows, $1/4 \times 2\text{-}1/8$-in. diam, sealed with neoprene O rings. A Dumont 6292 photomultiplier tube is mounted against each window with optical contact provided by mineral oil. The photomultiplier tubes are wired in parallel in two banks of 44 tubes each. Both banks observe all parts of the scintillator. A copper electrical shield is placed around the entire phototube assembly, making the total diam 48 in. Space for the telescope counters and the target assembly is provided by the 8-in. beam tube going through the middle of the tank (Fig. 5).

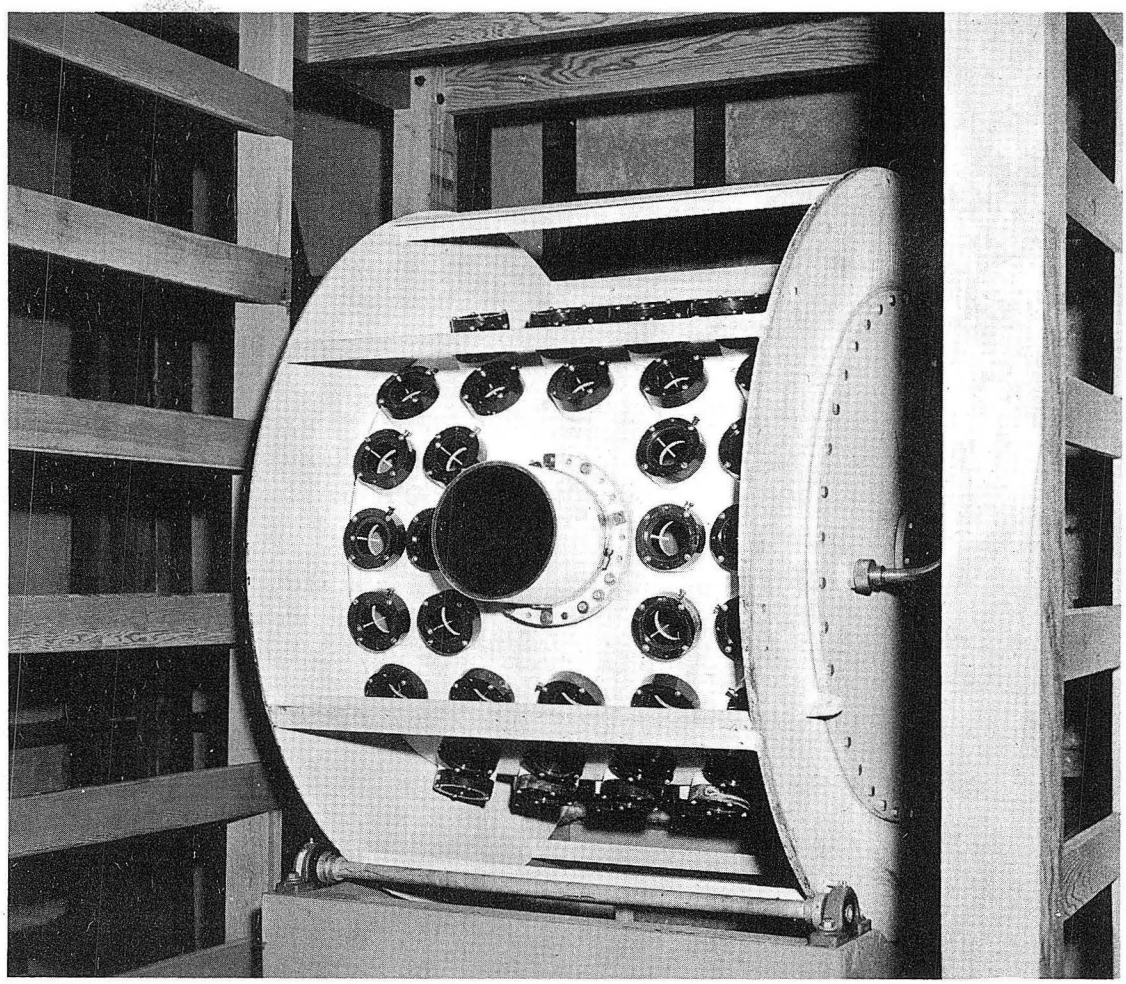

ZN-4387

Fig. 5. Close-up of the scintillator tank without phototubes, the surrounding copper electrical shielding, or the lead and boric acid shielding. For this experiment the tank was placed flat on one end.

The entire tank is completely surrounded with 2 in. of lead, with 0.5 in. of boric acid powder outside the lead (Fig. 2). The resulting apparatus was embedded in the shielding wall of the meson cave in order to reduce the background of neutrons from the cyclotron (Fig. 1).

2. Method of Neutron Detection

There is often a prompt tank pulse associated with a μ^--meson capture (Fig. 6). This can come from three sources:

a. x rays from the μ^- capture converting in the tank,

b. conversion of the γ radiation emitted by a still-excited nucleus after it was unable to emit further neutrons,

c. recoil protons from the thermalizing neutrons. Most of the neutrons entering the scintillator lose practically all their energy to recoil protons in much less than a microsecond, though not all become thermalized until after $\approx$ 4 μsec.

When thermalized, the neutrons are captured with a time constant which depends on the Cd/H ratio. The ratio of 0.0019 used here yields a tank time constant, after thermalizing, of 7.8 μsec (Fig. 7). The neutron is captured 95% of the time by Cd^{113} giving a cascade γ decay of 9.2 MeV,[4] and 5% of the time by H^1 giving a 2.2-MeV γ ray. This radiation, converting in the tank, yields a pulse indicating the neutron capture (Fig. 6).

3. Calibration of Efficiency

The tank neutron efficiency was calibrated often, at least once a day, with Cf^{252} in a fission chamber.[37] Cf^{252} gives off an average of 3.87± 0.08 neutrons per fission.[38] The cyclotron beam was turned off and the chamber was placed in the middle of the tank beam tube, replacing the target assembly. The amplified pulses from the fission chamber were used to trigger the oscilloscope and the tank display was photographed (Fig. 6). A fission chamber discriminator plateau was obtained and the discriminator bias was set so that no alpha pile up triggers were obtained, as shown by all traces' having a prompt pulse.

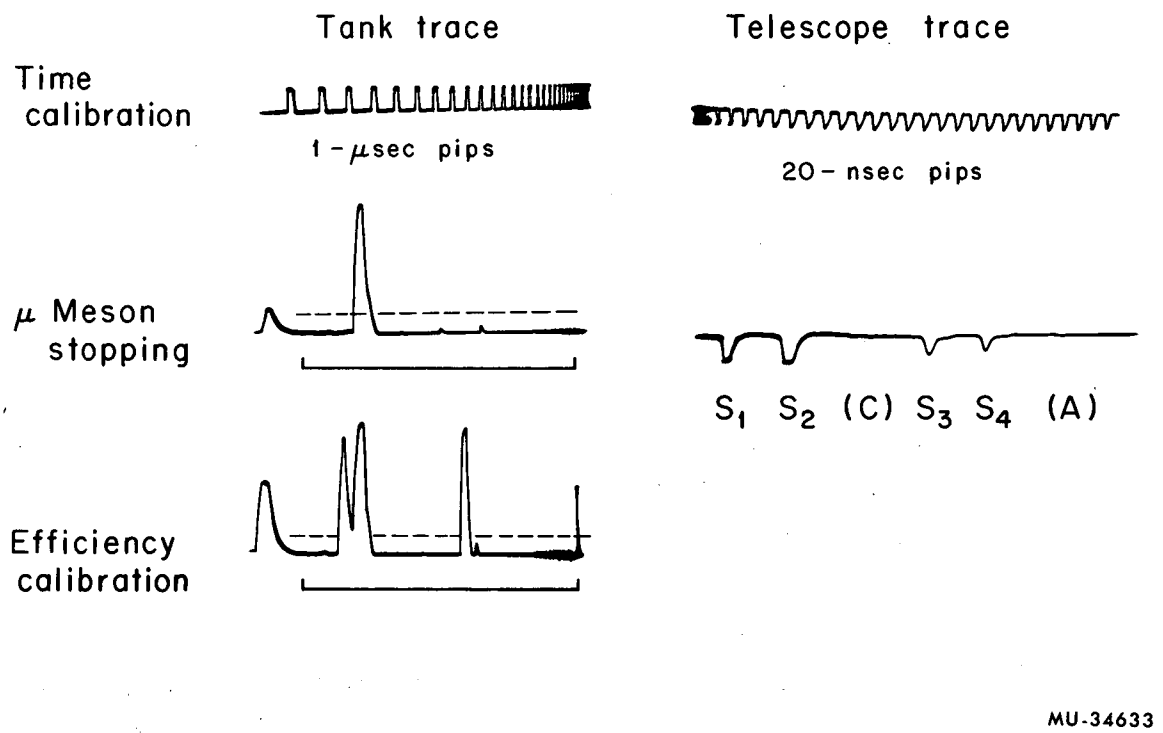

Fig. 6. Typical oscilloscope traces. For the tank trace, the bar represents the time during which neutron pulses were counted; the dotted line, the minimum height accepted. On the telescope trace a μ-meson stopping is signaled by the presence of pulses from counters S_2, S_3, and S_4, and the absence of Cerenkov- and anti-counter pulses (Č and A).

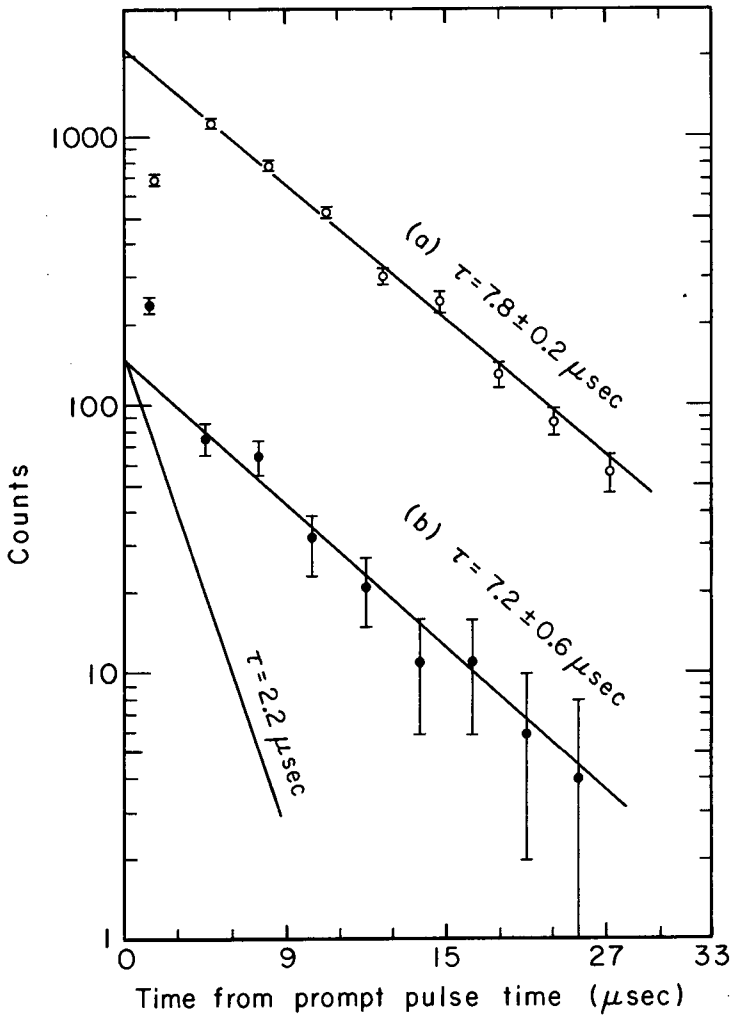

MU-34480

Fig. 7. Time distribution of delayed pulses from (a) Cf^{252} fission chamber calibration runs, and (b) μ^- stoppings in silicon. Background has been subtracted. The μ-meson lifetime is shown for comparison.

Background for the fission chamber runs was determined by using an independent trigger for the oscilloscope. This was about 0.03 pulse per 30-μsec sweep.

Using the fission chamber in this way to calibrate the efficiency of neutron detection indicates any changes or drifting in the entire system. During the course of the first cyclotron run a gradual increase in efficiency of about 5% was observed. The efficiency remained constant during the second cyclotron run.

There are several reasons for the tank efficiency to be less than 100%. Since neutrons were counted only up to 32 μsec after the prompt pulse, about 5% of the neutrons were captured after the sweep ended. Some neutrons escape directly out of the beam tube. Others escape before being captured. Some neutrons are captured but give a pulse of too small an energy to be observed.

For a slightly different geometry, Monte Carlo calculations indicate an energy dependence of the neutron-capture efficiency of the tank: 99% for 1-MeV neutrons, 95% for 3-MeV neutrons, 89% for 5-MeV neutrons, and 84% for 7-MeV neutrons.[37] This energy dependence does not have much effect in μ-meson capture, since most neutrons emitted are those from nuclear evaporation whose energy is mostly less than ≈ 3 MeV. In the Cf^{252} efficiency calibration each fission fragment evaporates on the average two neutrons. This implies a nuclear excitation of ≈10 MeV,[39] and an energy spectrum similar to evaporation neutrons from μ-meson capture.

C. Operation, Telescope, and Electronics

The experiment was performed in two separate cyclotron runs, 4 months apart. Data were taken in the first run for six targets: aluminum, iron, silver, iodine, gold, and lead. The second run was with silicon, calcium, and again with gold, as a check. The eight targets were chosen so as to span a wide range of atomic weights, to be monoisotopic if possible, and to furnish a check with Kaplan's previous cosmic-ray experiment. Targets were 7 in. in diameter. Thicknesses

were: Al, 2 in.; Si, 2 in.; Ca, 4 in.; Fe, 3/4 in.; Ag, 3/4 in.; I, 2 in.; Au, 13/16 in.; Pb, 3/4 in.

All counters were plastic scintillators except C, a 5X5X2-in. water Cerenkov counter with shifter (Fig. 2). S_1, S_2, and S_3 were 4 in. square by 1/4 in. thick. S_4 was 4 in. in diameter by 1/4 in. The anticounter, A, was 7 in. in diameter by 1/2 in. thick. All counters were viewed with RCA 6655A photomultiplier tubes except S_4, which had two RCA 1P21's because of space limitations. The neutron detector is treated separately in the following section.

The block diagram of electronics is given in Fig. 8. The beam was monitored with S_1 and S_2 in coincidence. Resolution times of coincidence circuits were typically 10 nanoseconds. Neutrons detected by the liquid scintillator tank following a μ capture were counted by two methods, as follows:

The sweeps of a four-gun scope, triggered by S_2, S_3, and S_4 in coincidence, were photographed. The amplified tank pulses were exhibited on one trace which had been modified so it had an exponential sweep, $x = x_0[1 - \exp(-t/\tau)]$. The time constant was set approximately equal to the tank's neutron capture time of 7.8 μsec in order to have an equal density of neutron pulses along the sweep. The total sweep length was 35 μsec. The other sweep contained the delayed and added outputs from the six counters exhibited in sequence (Fig. 6). Both sweeps were time-calibrated at intervals by use of a time-mark generator.

A stopping particle (S_2, S_3, and S_4 in coincidence, and the sum of C and A in anticoincidence) triggered a 30-μsec gate delayed by 2 μsec. Tank pulses from the linear amplifier were fed into a number-to-height converter which gave an output pulse proportional to the number of pulses occurring during the gate. This was put into a 10-channel pulse-height analyzer adjusted so that the nth channel registered the number of times exactly n tank pulses were detected following a stopping particle. This method gave immediate answers for neutron multiplicities for purposes of checking during the cyclotron runs. However, all results presented here are derived from the photographic data because of its superior time resolution and freedom from extraneous pulses.

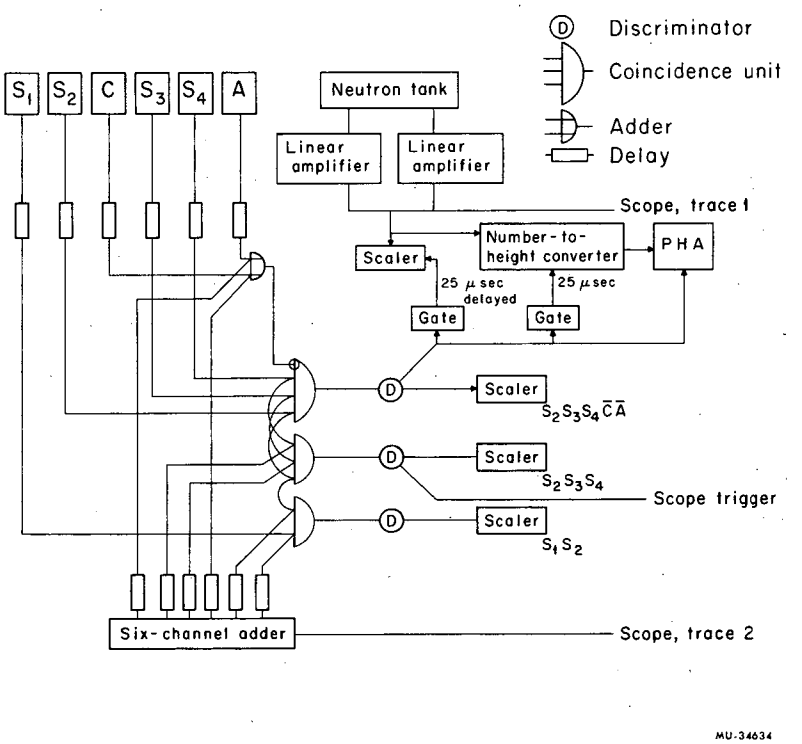

Fig. 8. Block diagram of electronics.

The beam level was reduced considerably in order not to have the scintillator tank background exceed more than about 0.1 pulse per 30-μsec gate. This background rate corresponded to a beam level of, roughly, 200 counts/min in the beam monitor or about two μ-meson stoppings per minute.

The tank background during target runs was continuously sampled by a scaler that counted for a 25 μsec gate that was delayed by 25 μsec from the beam monitor (S_1S_2) trigger. This was done so as to have an average background rate that reflected the time profile of the beam.

Target runs were generally alternated with background runs in order to correlate the continuous monitoring by the background counter and background pulses recorded on the film. For background runs the oscilloscope was triggered by a pulse delayed by 25 μsec from the S_1S_2 coincidence. Pulses recorded on the film thus represented an almost random sampling of background seen by the tank.

Several times, runs were made with no target in place in order to make a correction for μ's stopping in the last counter (S_4).

IV. DATA ANALYSIS

The data on film were converted to punched cards by use of a digitized scanning projector. Each event was analyzed by means of an IBM 650 computer program. The neutron tank trace gave the prompt pulse height and the height and time from the prompt-pulse time of any subsequent pulses; the telescope trace gave the times of telescope pulses present in order to classify the event. The time-mark-generator information provided the time scale.

Tank trace pulses were accepted for a gate time of about 30 μsec beginning a short time after the prompt-pulse time. This time delay was chosen larger for the three lightest elements (Table III) in order to reduce the fraction of μ-decay electrons occurring within the neutron gate. The choice of the minimum acceptable pulse height was influenced by the sharp rise in background for lower values (Fig. 9) and the lowering of neutron-detection efficiency for higher values (Fig. 10).

The time distribution of neutrons from the Cf^{252} fission chamber calibration runs is given in Fig. 7. (The first point is low because of the time taken for neutrons to thermalize.) Comparison of the fission chamber data with the time distribution of tank pulses from μ capture verifies that these pulses are due to neutrons.

For a given target run the average number of background pulses with height above the chosen value for a 30-μsec trace was found as follows. All background runs were combined for better statistics. The average number of background pulses per 30-μsec trace was determined from the film. This number was divided by the average background (as measured by the background counter). This ratio gave the calibration of the film background in terms of the background counter. The film background on a given target run was then taken to be this ratio times the particular reading of the background counter for this run. The average film background per 30 μsec for background runs was actually determined on the basis of the last half of the sweep only, since there was

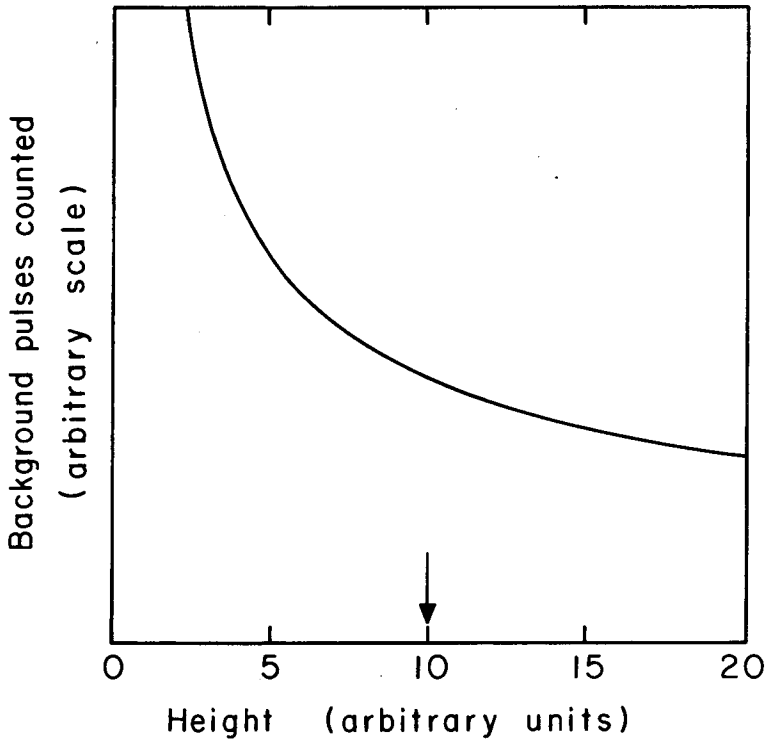

MU-34481

Fig. 9. Pulse-height distribution for background runs. The arrow indicates the pulse height chosen.

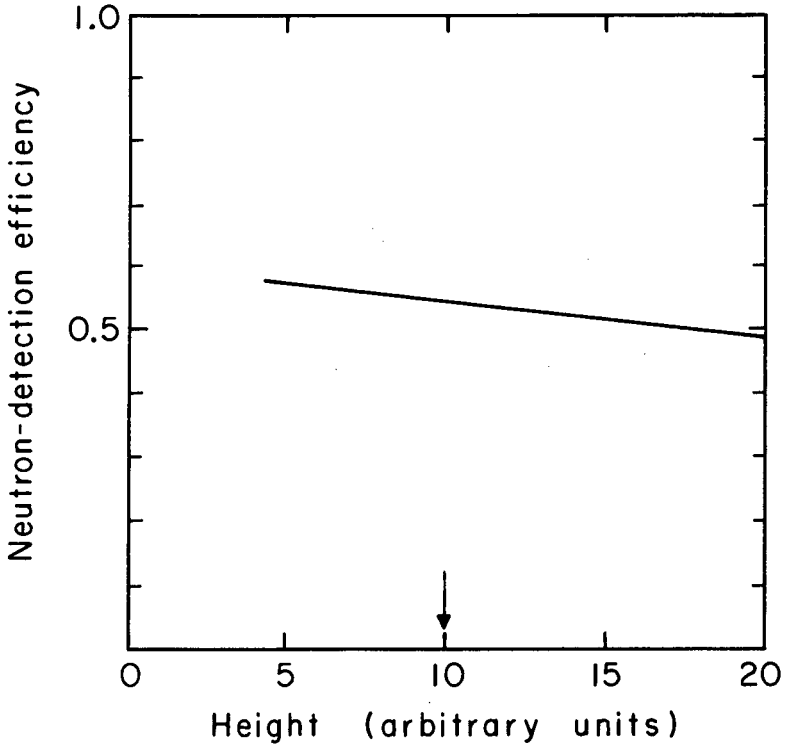

MU-34482

Fig. 10. Tank efficiency as a function of pulse height. The arrow indicates the pulse height chosen.

some time dependence of background pulses. (In Fig. 11 the decrease in measured background at 30 μsec is due to a lower scanning efficiency at the end of the sweep.) This time dependence is attributed to our method of triggering for background runs with the beam monitor and delaying only 25 μsec before counting, so that we included some pulses associated with captures. (A much longer delay would have put too many of the traces outside the 400-μsec beam spill.) Measurements of the number distribution of these background pulses indicated that the background was statistically independent (Poisson-distributed).

A background correction to the measured multiplicity distribution (F_0, F_1, $\cdots$), was made for every target run (see Appendix for the method). Data for a given target were taken in, typically, 12 runs with varying background rates, β. Runs for the same target were then combined and adjusted to the same efficiency, $e = 0.545$, by Eq. (10). Results are not converted to 100% efficiency because of the large statistical fluctuations obtained in the higher multiplicities. A target-out correction was made. The fraction of μ's not stopping in the target was determined to be 0.068 ± 0.012 for the first cyclotron run, and 0.077 ± 0.015 for the second. The final correction was for the decay of the μ meson. The fraction that decays instead of being captured is λ_d/λ (Table I) where λ_d is the decay rate, and the total disappearance rate, λ, is the sum of λ_d and the capture rate, λ_c. A further correction in aluminum and silicon was made for decay electrons detected during the neutron gate. The fraction of captures with detectable electrons is 0.059 in aluminum and 0.049 in silicon. A tank detection efficiency of 0.80 ± 0.20 for electrons was assumed.

Errors quoted are statistical and do not include systematic errors if present (other than the small error in aluminum and silicon from the assumed electron efficiency above). Errors were propagated through the various corrections. For better accuracy, average multiplicities and their errors were calculated separately from the multiplicity distributions. Statistical errors for the background subtraction, found as described in the Appendix, were due to counting statistics and to variations

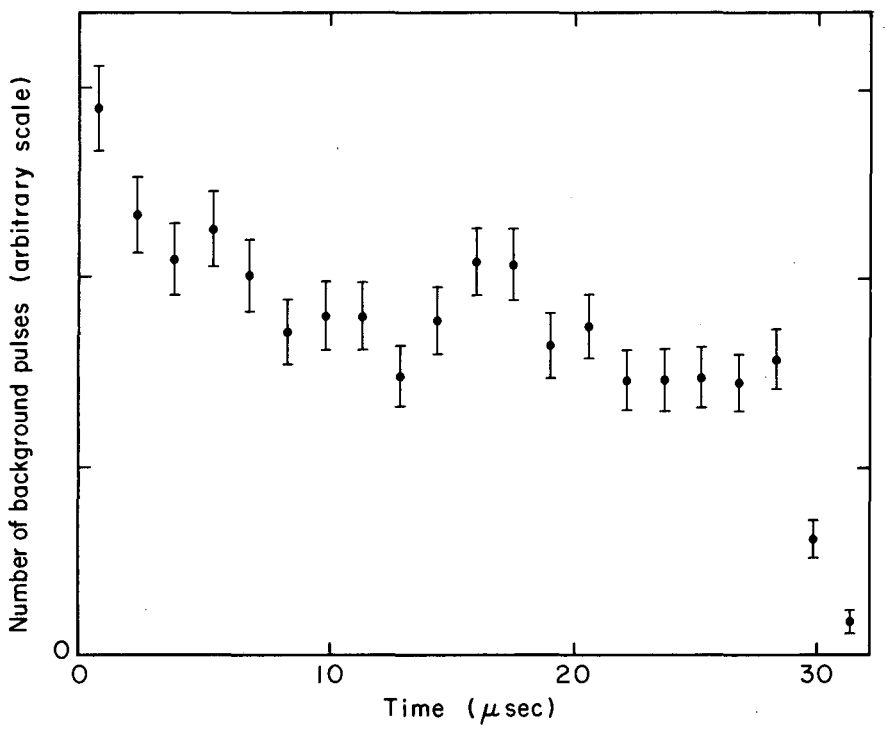

MU-34484

Fig. 11. Time distribution of background pulses averaged over targets.

of background within a given run because of beam level variations. If the background rate is $\beta \pm \sigma$, then β was generally about 0.1 pulse per 30-μsec sweep and σ was taken to be 0.01 pulse per sweep. The contribution of σ to the error turned out to be small. The errors quoted in the results (Table IV) follow from taking the square root of the diagonal terms of the background-subtraction covariant matrix.

V. RESULTS AND DISCUSSION

A. Experimental Results

Values of the experimentally observed neutron multiplicities are given in Table III. The data, with background, target-out, and decay corrections, reduced to a common detection efficiency (0.545), are given in Table IV. The reduced data for gold from the two different cyclotron runs have been combined, since their agreement was within that expected from statistics.

B. Comparison with Other Experiments

A summary of previous experimental results for average multiplicities for our targets is given in Table V. Our results are in agreement with these, within their stated errors, except for Widgoff's values for aluminum and lead. Widgoff has estimated that her results may have a systematic error as high as 20% because of the difference between the neutron energy spectrum from μ capture and from the Ra-Be source used in her calibration. This does not account for the disagreement in aluminum.

The only previous determination of neutron multiplicity distributions done with high efficiency is from the cosmic-ray experiment of Kaplan et al.[5] The experiment presented here has used the same neutron detector and fission-chamber calibration method. Their results, adjusted to our detection efficiency, are given at the bottom of Table IV. The agreement is good, both for the average neutron emission and for the multiplicity distribution.

C. Comparison of Experiment with Theory

The following results involving calculations of neutron emission are given without including effects of direct emission and of the nuclear surface, since it is not clear in all cases what these corrections should be. (Calculations of direct emission for calcium range from 25%, by

Table III. Uncorrected data.

Target	Neutron gate (μsec)	Efficiency	Average background (pulses per 30-μsec sweep)	Total events	Multiplicity distribution						
					F_0	F_1	F_2	F_3	F_4	F_5	F_6
Al	2.5 to 31.0	0.495±.014	0.102	1492	912	471	81	26	1	0	1
Si[a]	2.5 to 29.5	0.553±.015	0.082	657	439	186	28	1	1	1	1
Ca[a]	2.5 to 29.5	0.553±.015	0.078	1846	1154	605	73	10	4	0	0
Fe	1.5 to 31.0	0.545±.015	0.105	1426	705	559	132	26	2	2	0
Ag	1.5 to 31.0	0.545±.015	0.129	897	317	384	146	38	9	2	1
I	1.5 to 31.0	0.545±.015	0.122	909	351	405	108	35	9	1	0
Au	1.5 to 31.0	0.545±.015	0.114	1192	408	510	198	52	19	4	1
Au[a]	1.5 to 29.5	0.608±.017	0.097	535	201	199	101	22	9	3	0
Pb	1.5 to 31.0	0.545±.015	0.117	720	235	325	113	37	10	0	0
Target out	1.5 to 31.0	0.545±.015	0.093	30	18	12					
Target out[a]	1.5 to 29.5	0.599±.017	0.089	25	12	13					

[a] Data taken during the second cyclotron run.

Table IV. Corrected experimental results adjusted to 0.545 efficiency.

Target	Average multiplicity, $\langle n \rangle$	Multiplicity distributions							
		F_0	F_1	F_2	F_3	F_4	F_5	F_6	F_7
Al	1.262±.059	0.449±.027	0.464±.028	0.052±.013	0.036±.007				
Si	0.864±.072	0.611±.042	0.338±.042	0.045±.018	-0.002±.008	0.003±.005	0.002±.005	0.003±.006	
Ca	0.746±.032	0.633±.021	0.335±.022	0.025±.009	0.004±.006	0.003±.003			
Fe	1.125±.041	0.495±.018	0.416±.019	0.074±.011	0.014±.005				
Ag	1.615±.060	0.360±.021	0.456±.023	0.144±.017	0.031±.009	0.007±.005	0.002±.004		
I	1.436±.056	0.396±.021	0.474±.023	0.087±.015	0.035±.009	0.007±.005			
Au	1.662±.044	0.370±.015	0.425±.016	0.156±.012	0.032±.006	0.014±.004	0.003±.003		
Pb	1.709±.066	0.324±.022	0.483±.025	0.137±.018	0.045±.010	0.011±.006			
Previous results of Kaplan, Moyer, and Pyle (reference 5), adjusted to 0.545 efficiency.									
Ag	1.60±.18	0.389±.100	0.455±.075	0.120±.035	0.030±.015	0.001±.003	0.009±.006	0.000±.007	0.010±.007
Pb	1.64±.16	0.348±.100	0.479±.057	0.137±.027	0.018±.012	0.010±.005	0.005±.004	0.003±.002	0.002±.002

Table V. Average neutron multiplicities--previous experimental results.

Element	Average multiplicity	Source (from reference 11)
Al	0.95± 0.17	Widgoff (1953)
Ca	0.40± 0.4	Conforto and Sard (1952)
Ag	1.60± 0.18	Kaplan, Moyer, and Pyle (1958)
I	1.7 ± 0.4	Winsberg (1954)
Pb	2.0 ± 0.7	Groetzinger et al. (1951)
Pb	2.1 ± 0.5	Crouch and Sard (1952)
Pb	1.5 ± 0.4	Conforto and Sard (1952)
Pb	2.14± 0.13	Widgoff (1953)
Pb	1.5 ± 0.4	Jones (1957)
Pb	1.64± 0.16	Kaplan, Moyer, and Pyle (1958)

Dolinsky and Blokhintsev,[40] to ≈2%, inferred from Lubkin.[41]) Results that include Singer's direct-emission and nuclear surface corrections are given at the end.

We have investigated two forms of the nuclear momentum distribution, a Gaussian and a Fermi-gas, in our model of neutron emission from μ^- capture. The Gaussian distribution, $\exp(-p^2/\alpha^2)$, has been fitted to the nucleon momentum distribution from a number of experiments, with $\alpha^2/2M$ ranging from 14 MeV to 20 MeV. The value of 14 MeV is derived by Brueckner et al.[16] for processes involving high-momentum components, while 20 MeV is obtained by Azhgirey et al.[21] for quasi-elastic scattering, which involves low-momentum components. Since these latter are those involved in the nuclear excitations here, we have exhibited in more detail the Gaussian distribution results with $\alpha^2/2M = 20$ MeV. A Fermi-gas distribution with $\theta_f = 8$ MeV was also chosen because it gives a momentum distribution similar to the 20-MeV Gaussian (Fig. 12). A completely degenerate Fermi-gas distribution is also plotted.

For the Gaussian distribution, the model cannot yield the experimental value for the average multiplicity with the effective mass equal to the unbound nucleon mass (except for calcium) for any value of $\alpha^2/2M$ that also fits the experiments on nucleon momentum distributions[19-21] (that is, for 14 MeV $\leq \alpha^2/2M \leq$ 20 MeV). For the Fermi-gas momentum distribution the model can give the experimental $\langle n \rangle$ with $M^* = M$, but only (for the heavier elements, iron, silver, iodine, gold, and lead) for excitation temperatures well over 70 MeV. These temperatures imply momentum distributions markedly different from those which have been observed.

There are two model parameters we can vary: (a) the momentum distribution width, $\alpha^2/2M$ for the Gaussian or θ_f for the Fermi gas, and (b) the nucleon effective mass, M^*.

In comparing the model with experiment we first chose a value of effective mass that gave agreement with our measured values of $\langle n \rangle$. For this M^* a comparison was then made of the predicted multiplicity

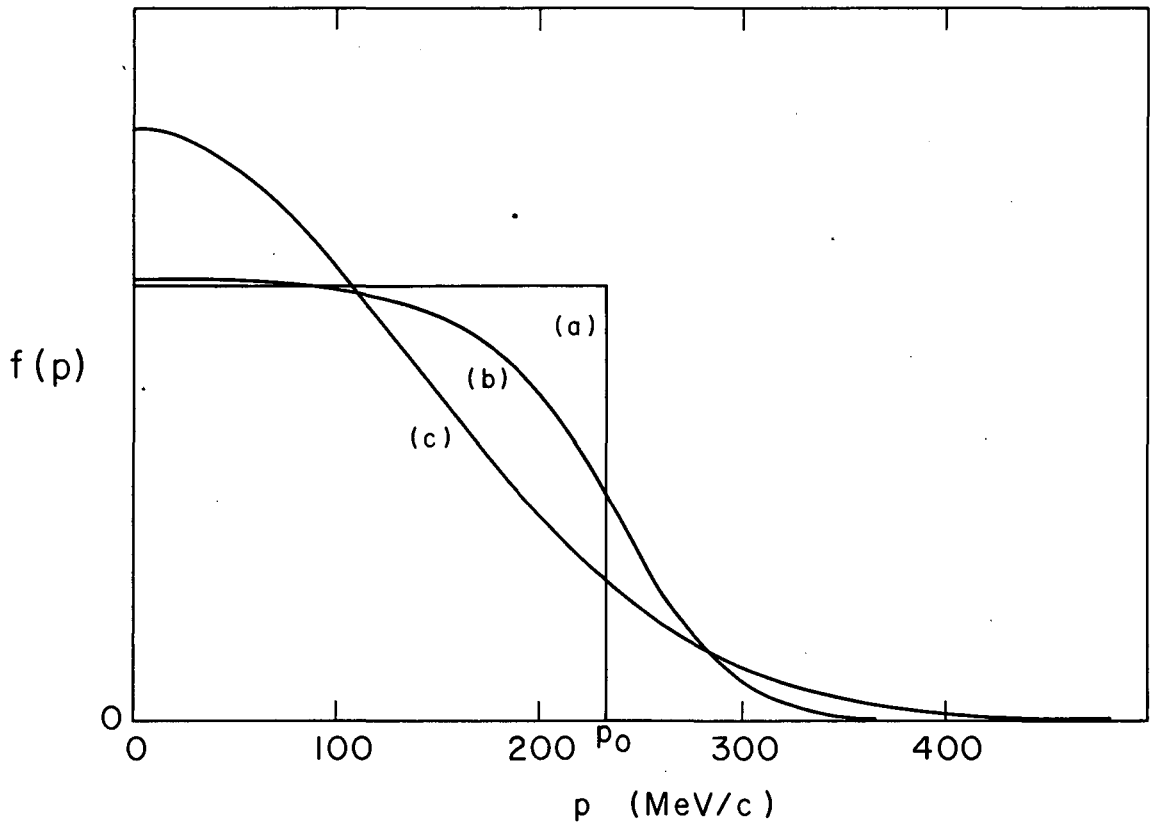

MUB-2675

Fig. 12. Nucleon momentum distributions. (a) Fermi gas (gold), θ_f = 0 MeV; (b) Fermi gas (gold), θ_f = 8 MeV; (c) Gaussian, $\alpha^2/2M$ = 20 MeV.

distribution, $(P_0, P_1, \cdots)$, with the measured values, $(F_0 \pm \delta F_0, F_1 \pm \delta F_1, \cdots)$, and the standard goodness-of-fit parameter, χ^2, was determined:

$$\chi^2 = \sum_n [(P_n - F_n)/\delta F_n]^2 .$$

(χ^2 was generally associated with three to four degrees of freedom.)

Figure 13 gives the nuclear excitation distribution, $I(Q)$, for the three momentum distributions chosen. Since, in each case, a value of effective mass has been chosen to give the experimental $\langle n \rangle$, the average nuclear excitations for the three curves have substantially the same value.

These values of effective mass and values of χ^2 were calculated for a wide range of momentum-width parameters (θ_f and $a^2/2M$). Results are given for all targets (Figs. 14-21). Because χ^2 is not a sensitive function of the momentum width, the model cannot determine both the effective mass and the momentum distribution width. We must rely on the results of other experiments for the momentum distribution.

M^*/M, χ^2, and the predicted multiplicity distributions for a Fermi-gas distribution with $\theta_f = 0$ and 8 MeV are given in Tables VI and VII. The fit with the observed multiplicity distribution is not good, except for silicon and calcium, which give good fits for all $\theta_f > 7$-10 MeV (Figs. 15, 16). (For example, a value of χ^2 of ≈ 3.4 for four degrees of freedom has a probability of 50% that chance gives no better fit.) In Figs. 14-21 the completely degenerate Fermi gas never gives the best fit, though only for Si, Ca, Fe, and Au is the effect marked. The five heavier elements show a minimum in χ^2 for $\theta_f \approx 2$ MeV. However, the exact shape of the χ^2 curves depends on the assignment of errors, which are not known precisely.

The Gaussian momentum distribution results with $a^2/2M = 20$ MeV are given in Table VIII. Multiplicity distributions are fitted well by this model for silicon and calcium, but not for the other elements.

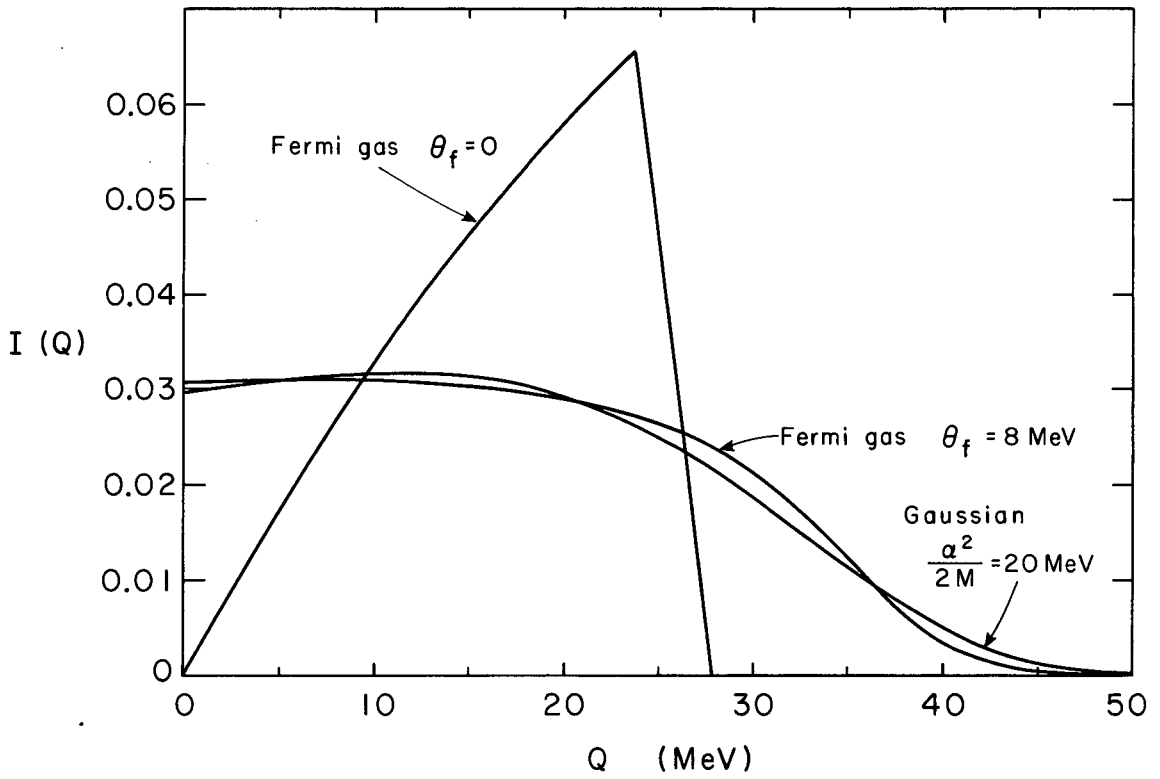

MUB-2676

Fig. 13. Nuclear excitation distribution from μ^- capture in gold. The effective mass in each case has been chosen so as to give the experimental average multiplicity.

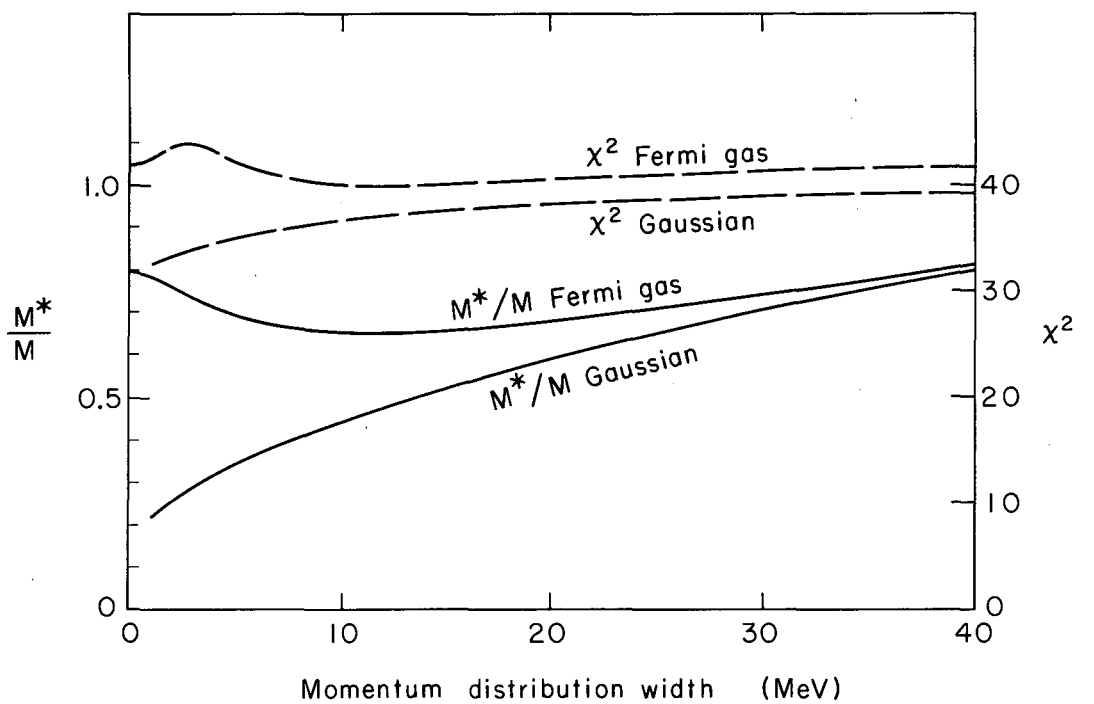

Fig. 14. Aluminum. The effective mass, M^*, required to give the experimental $\langle n \rangle$, and the corresponding fit (χ^2) with the experimental multiplicity distribution, as functions of the momentum width parameter (θ_f for Fermi gas or $a^2/2M$ for the Gaussian).

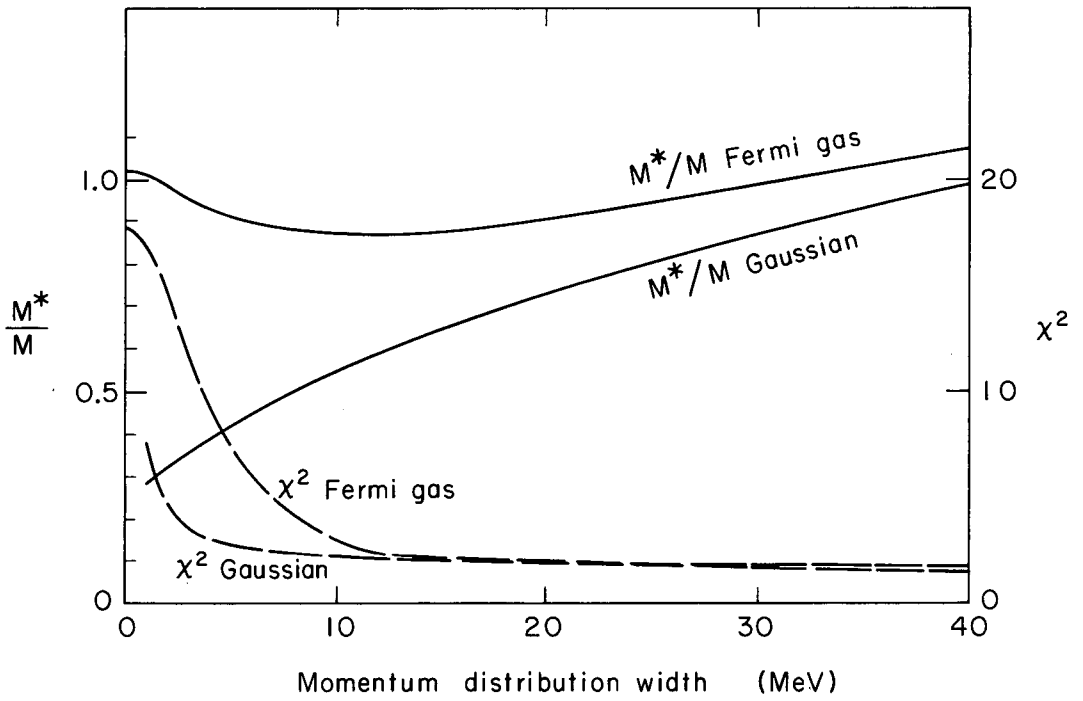

MU-34486

Fig. 15. Silicon. The effective mass, M^*, required to give the experimental $\langle n \rangle$, and the corresponding fit (χ^2) with the experimental multiplicity distribution, as functions of the momentum width parameter (θ_f for Fermi gas or $\alpha^2/2M$ for the Gaussian).

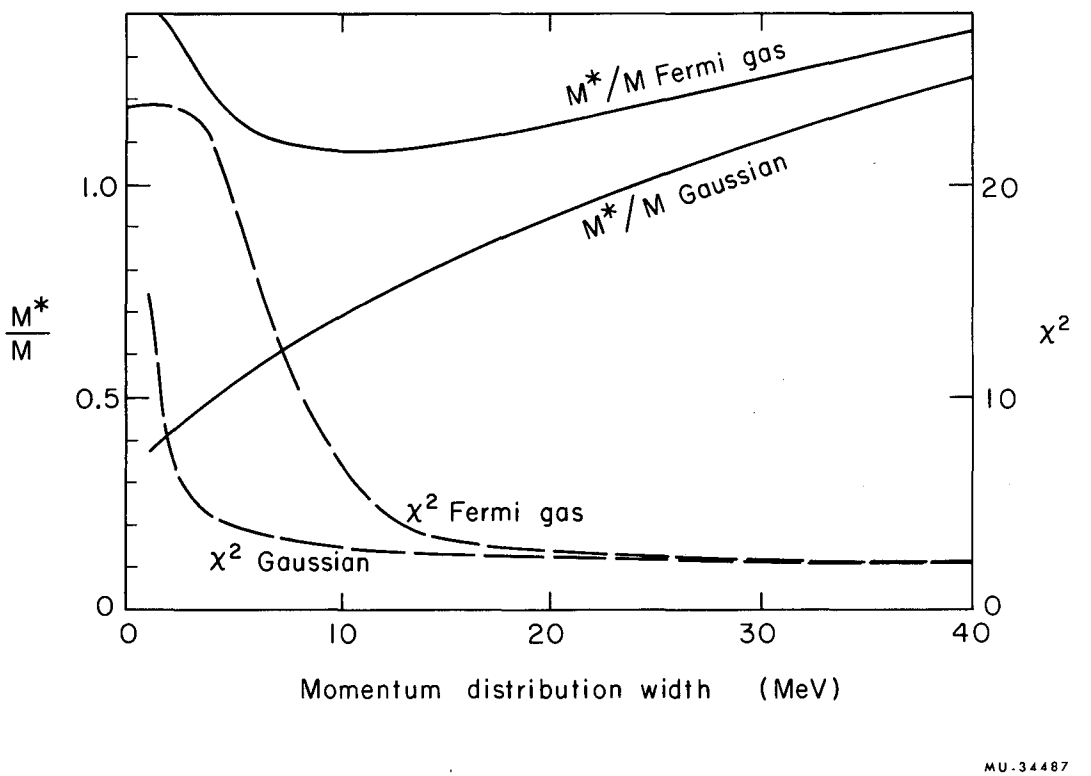

Fig. 16. Calcium. The effective mass, M^*, required to give the experimental $\langle n \rangle$, and the corresponding fit (χ^2) with the experimental multiplicity distribution, as functions of the momentum width parameter (θ_f for Fermi gas or $\alpha^2/2M$ for the Gaussian).

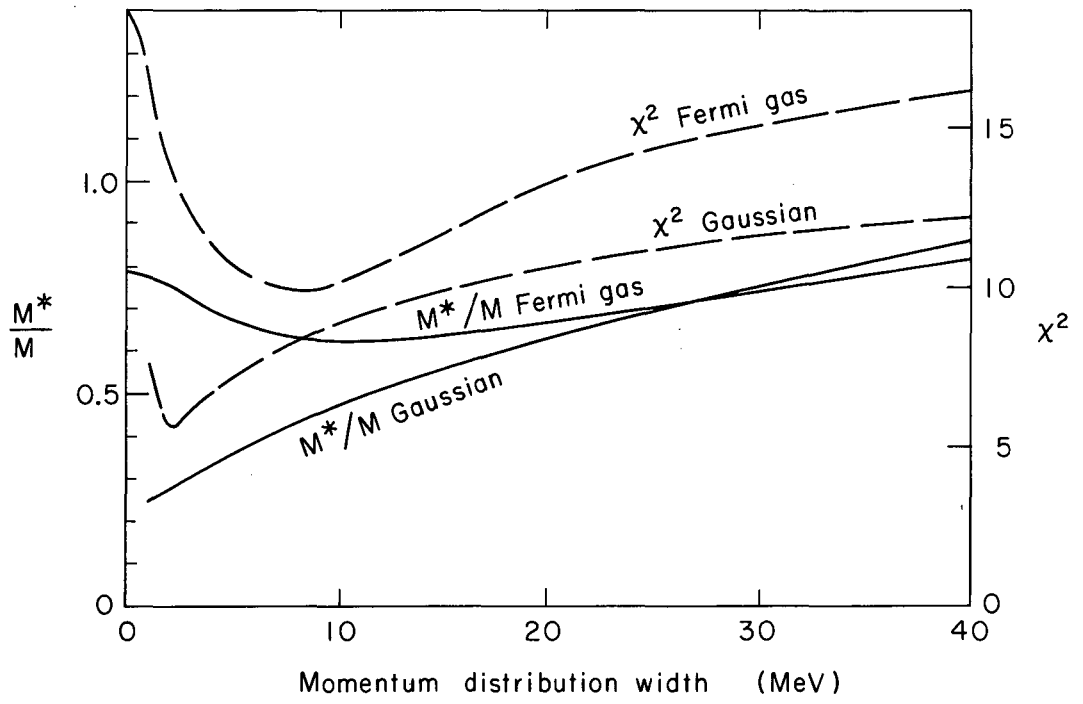

MU-34488

Fig. 17. Iron. The effective mass, M^*, required to give the experimental $\langle n \rangle$, and the corresponding fit (χ^2) with the experimental multiplicity distribution, as functions of the momentum width parameter (θ_f for the Fermi gas or $a^2/2M$ for the Gaussian).

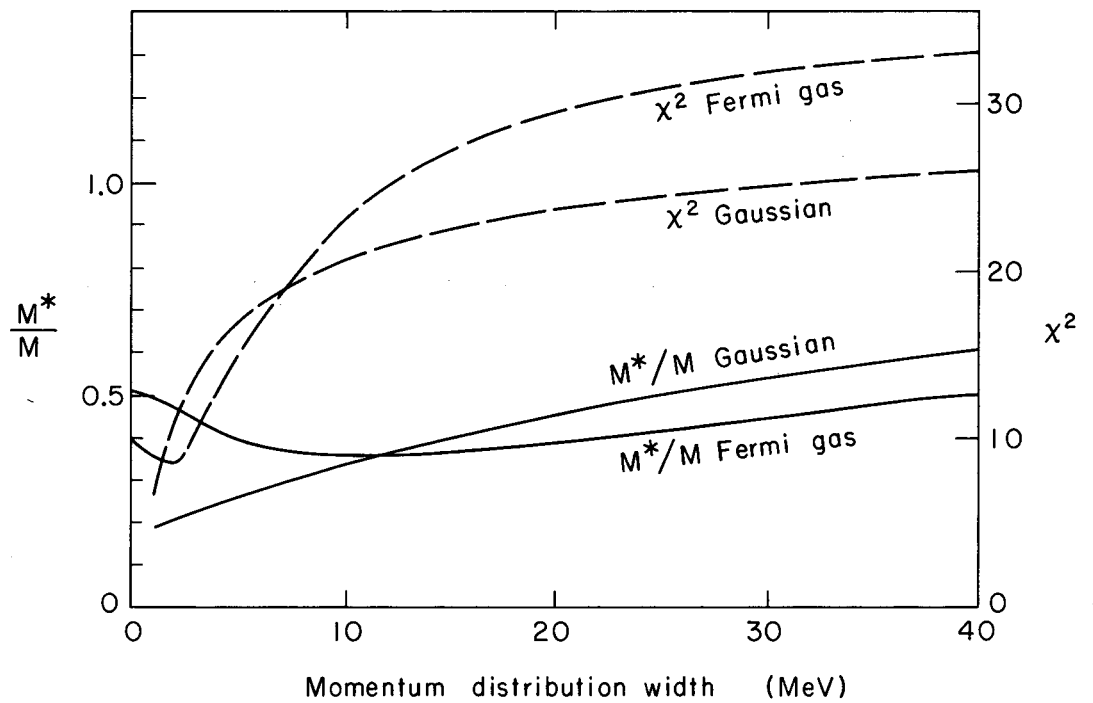

MU-34489

Fig. 18. Silver. The effective mass, M^*, required to give the experimental $\langle n \rangle$, and the corresponding fit (χ^2) with the experimental multiplicity distribution, as functions of the momentum width parameter (θ_f for Fermi gas or $a^2/2M$ for the Gaussian).

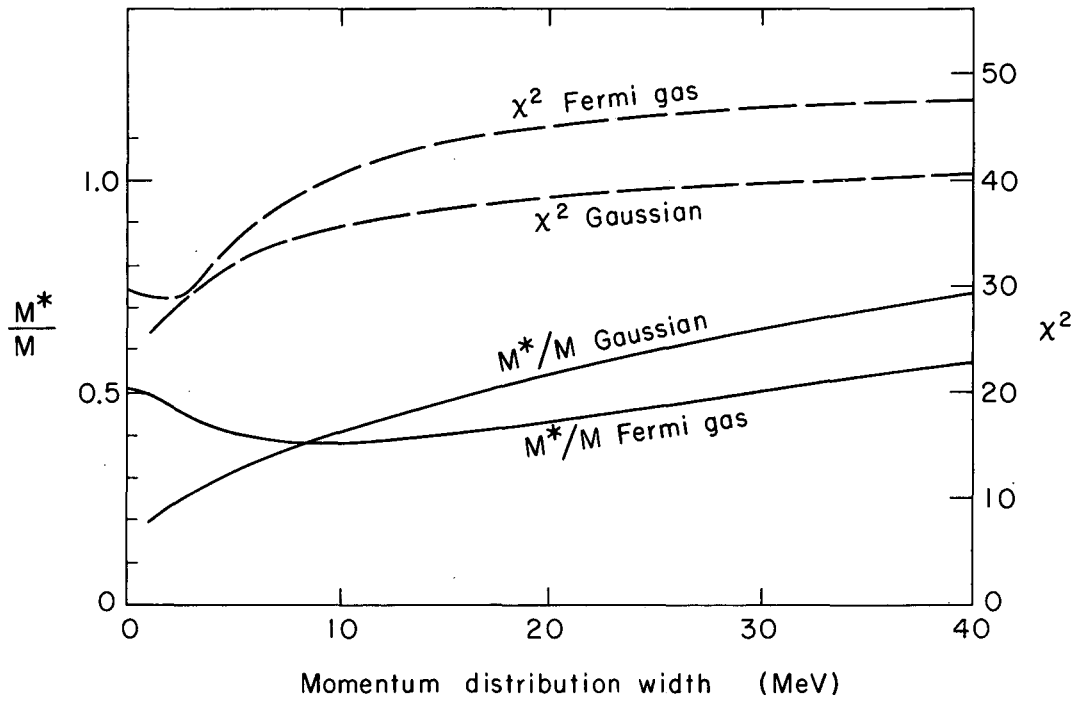

MU-34490

Fig. 19. Iodine. The effective mass, M^*, required to give the experimental $\langle n \rangle$, and the corresponding fit (χ^2) with the experimental multiplicity distribution, as functions of the momentum width parameter (θ_f for Fermi gas or $\alpha^2/2M$ for the Gaussian).

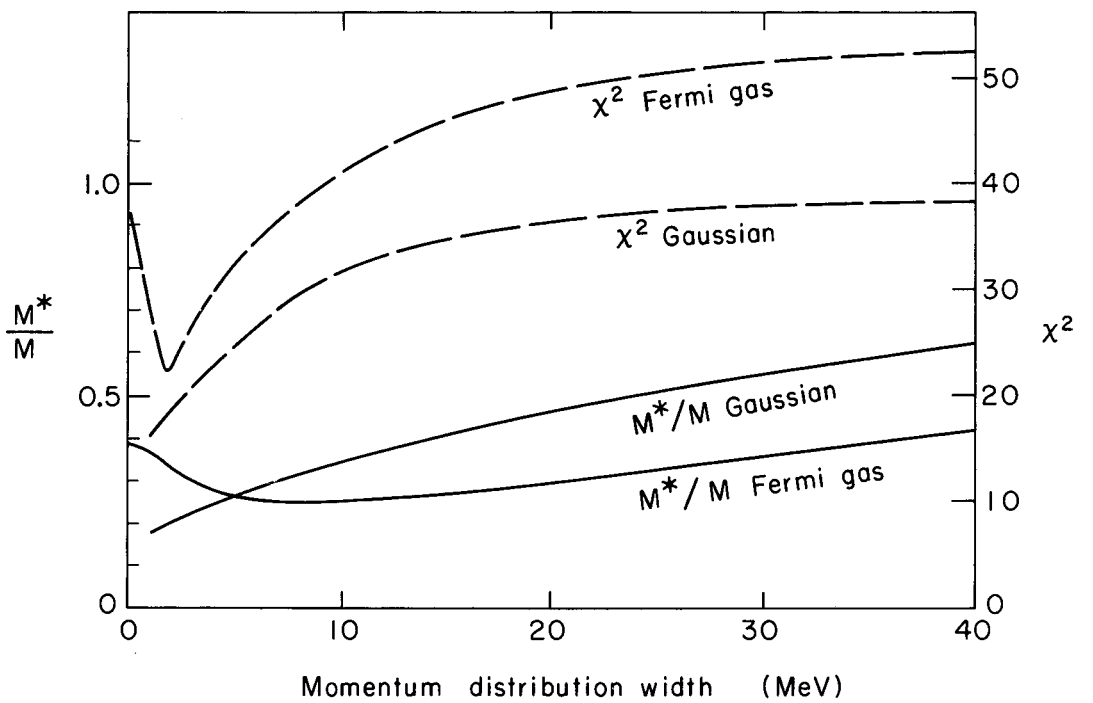

MU-34491

Fig. 20. The effective mass, M^*, required to give the experimental $\langle n \rangle$, and the corresponding fit (χ^2) with the experimental multiplicity distribution, as functions of the momentum width parameter (θ_f for Fermi gas or $\alpha^2/2M$ for the Gaussian).

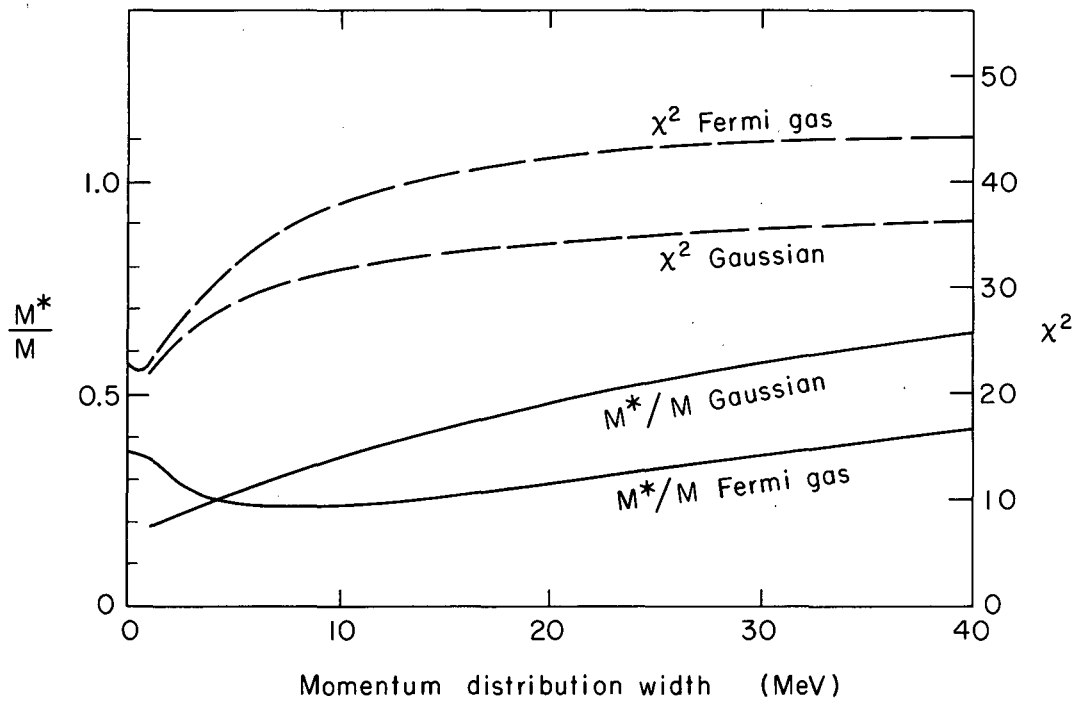

MU-34492

Fig. 21. Lead. The effective mass, M^*, required to give the experimental $\langle n \rangle$, and the corresponding fit (χ^2) with the experimental multiplicity distribution, as functions of the momentum width parameter (θ_f for Fermi gas or $a^2/2M$ for the Gaussian).

Table VI. Fermi gas distribution, $\theta_f = 0$ MeV. The effective mass that gives the experimental average multiplicity, χ^2, and the predicted multiplicity distribution. Effective mass values derived from values of nuclear level densities.

Target	Effective mass, M^*/M	χ^2	Multiplicity distribution P_0	P_1	P_2	P_3	Effective mass from level densities M^*/M
Al	0.794	41.9	0.415	0.483	0.102		0.449
Si	1.014	17.6	0.534	0.461	0.005		
Ca	1.444	23.6	0.593	0.407			
Fe	0.785	18.8	0.460	0.467	0.073		
Ag	0.501	9.9	0.337	0.464	0.180	0.019	0.62 to 0.77
I	0.507	29.5	0.375	0.473	0.147	0.005	0.541
Au	0.384	37.0	0.329	0.459	0.190	0.022	0.394
Pb	0.366	22.9	0.315	0.461	0.202	0.022	

Table VII. Fermi gas distribution, $\theta_f = 8$ MeV. The effective mass that gives the experimental average multiplicities, χ^2, and the predicted multiplicity distribution.

Target	Effective mass, M^*/M	χ^2	Multiplicity distribution				
			P_0	P_1	P_2	P_3	P_4
Al	0.62	40.5	0.455	0.415	0.118	0.012	
Si	0.878	4.3	0.565	0.400	0.035		
Ca	1.091	10.5	0.605	0.383	0.012		
Fe	0.629	9.9	0.495	0.400	0.100	0.004	
Ag	0.360	20.4	0.394	0.381	0.177	0.045	0.003
I	0.380	38.3	0.433	0.384	0.151	0.031	0.001
Au	0.246	38.1	0.395	0.367	0.180	0.052	0.005
Pb	0.230	36.1	0.382	0.371	0.187	0.053	0.006

Table VIII. Gaussian distribution, $a^2/2M = 20$ MeV. The effective mass that gives the experimental average multiplicity, χ^2, and the predicted multiplicity distribution.

Target	Effective mass, M^*/M	χ^2	Multiplicity distribution					
			P_0	P_1	P_2	P_3	P_4	P_5
Al	0.588	38.0	0.469	0.393	0.118	0.020		
Si	0.730	1.9	0.579	0.372	0.048	0.001		
Ca	0.923	2.5	0.621	0.352	0.027			
Fe	0.627	10.6	0.510	0.379	0.100	0.011		
Ag	0.449	23.6	0.404	0.373	0.169	0.048		
I	0.542	38.3	0.440	0.377	0.146	0.034	0.003	
Au	0.461	36.4	0.399	0.366	0.175	0.053	0.007	0.001
Pb	0.480	34.5	0.383	0.372	0.183	0.053	0.008	

The better fit for silicon and calcium is probably due to their lower average neutron multiplicity. Lower values of $\langle n \rangle$ imply smaller values of multiplicities of two or higher for the predicted distributions. Direct emission and clustering corrections to the distribution affect mostly these multiplicities, and would not appreciably change the fit with experiment if they are small. For all elements, χ^2 is essentially constant for $a^2/2M$ from 14 to 20 MeV, while M^* generally increases by $\approx 15\%$ in the same range (Figs. 14-21). A comparison of the 20-MeV Gaussian and the experimental multiplicity distributions is given in Figs. 22 and 23.

A quantity of interest is the average nuclear excitation, $\langle Q \rangle$. If $\langle n \rangle$ is plotted as a function of $\langle Q \rangle$--for calcium, for example (Fig. 24)-- for both the Fermi gas and Gaussian momentum distributions we get very nearly a straight line. Lower values of the effective mass are associated with higher values of $\langle Q \rangle$. Variations of the neutron boil-off temperature, the nuclear radius, θ_f, or a give straight lines quite close to each other. (The completely degenerate Fermi gas does not fit the line well, but it also does not in general give as good a fit to the multiplicity distributions as does the nondegenerate gas.) Thus the relationship between $\langle n \rangle$ and $\langle Q \rangle$ is not very sensitive to the distribution used or to the value of effective mass. Values of $\langle Q \rangle$ determined from our experimental values of $\langle n \rangle$ are given in Table IX. The statistical uncertainty in $\langle Q \rangle$ is less than ± 1 MeV (except for silicon: ± 2 MeV). The uncertainty due to the model is probably not more than ± 1 MeV. Since the average neutrino momentum occurs in a very important way in calculations of μ-meson capture rates in nuclei,[42] the (linear) average of this momentum, $\langle kc \rangle = E_0 - \langle Q \rangle$, is also given (Table IX). When $\langle kc \rangle$ is expressed in units of the reduced muon mass, $\mu' c^2 = \mu c^2 - B_\mu$, it has a striking uniformity over a wide range of Z (except for calcium).

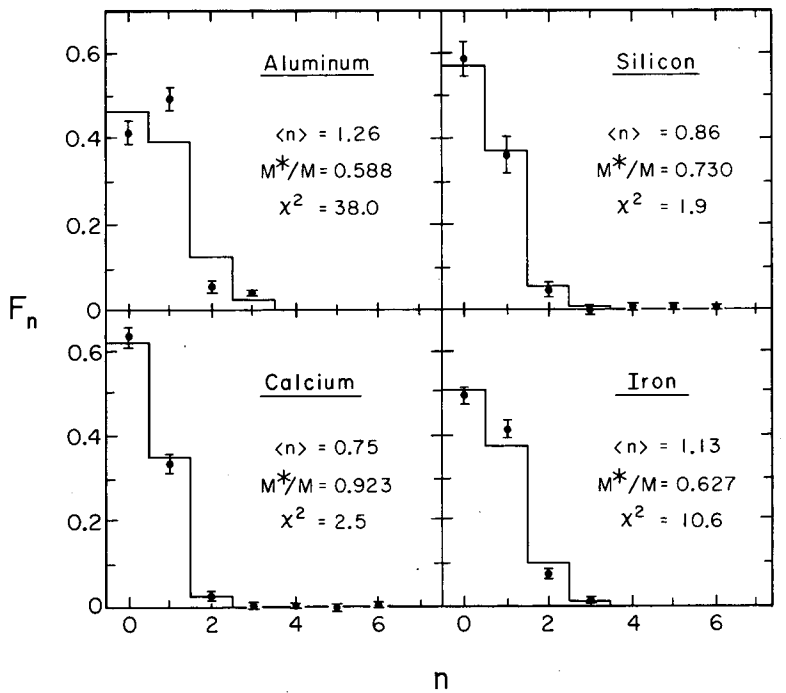

Fig. 22. Comparison of the observed neutron multiplicities with histograms calculated by using the Gaussian momentum distribution, $\alpha^2/2M = 20$ MeV. For aluminum, silicon, calcium and iron.

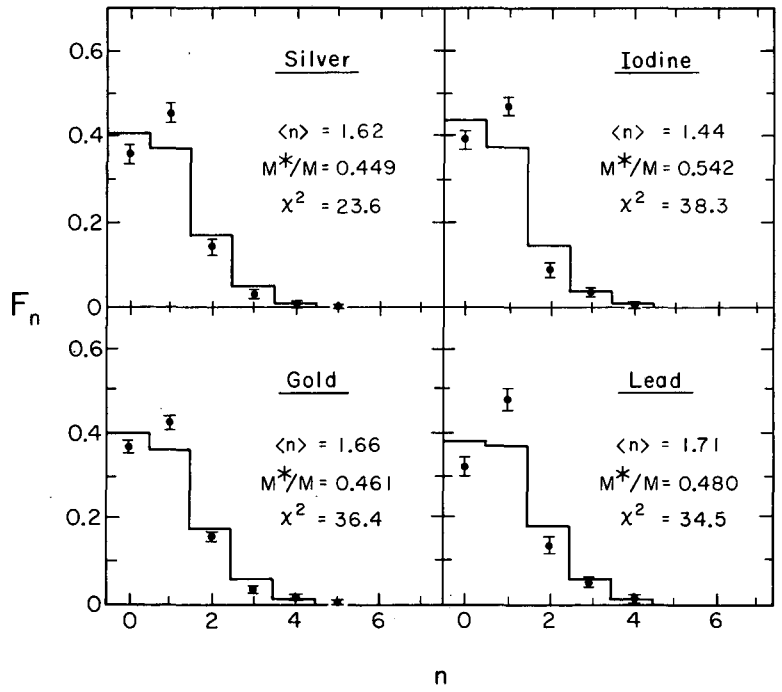

Fig. 23. Comparison of the observed neutron multiplicities with histograms calculated by using the Gaussian momentum distribution, $\alpha^2/2M$ = 20 MeV. For silver, iodine, gold, and lead.

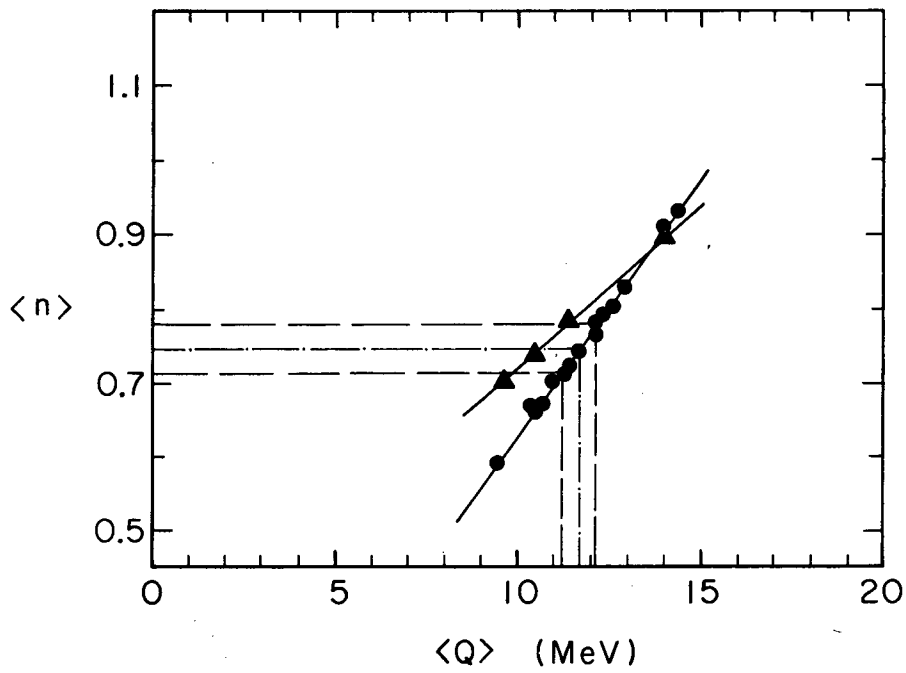

MU-34483

Fig. 24. Relationship between the average neutron multiplicity and the average nuclear excitation for calcium. ▲, Degenerate Fermi gas; ●, Nondegenerate Fermi gas and Gaussian, with θ ranging from 8 to 40 MeV.

Table IX. Maximum energy, average nuclear excitation, and average neutrino momentum.

Target	Maximum excitation, E_0 (MeV)	Average excitation, $\langle Q \rangle$ (MeV)	Average neutrino momentum $\langle kc \rangle$ (MeV)	$\langle kc \rangle / \mu' c^2$
Al	102.1	15.5	86.6	0.82
Si	100.0	13.3	86.7	0.82
Ca	102.8	11.7	91.1	0.87
Fe	99.7	14.5	85.2	0.82
Ag	99.8	17.5	82.3	0.82
I	98.7	15.6	83.0	0.83
Au	94.3	16.3	78.0	0.82
Pb	91.2	15.4	75.8	0.80

The harmonic oscillator shell-model calculation of the excitation of Ca^{40} (Fig. 25) gives a value for the average multiplicity, $\langle n \rangle = 0.744$, which is in good agreement with the experimental, $\langle n \rangle = 0.746 \pm 0.032$. The calculated average excitation, $\langle Q \rangle = 11.15$ MeV, is close to $\langle Q \rangle = 11.6$ MeV, derived from the Fermi-gas and Gaussian models and the measured $\langle n \rangle$. The agreement of this shell-model calculation is interesting, but is proably accidental, since the threshold for emission of the first neutron $[Q = M(Z-1, A)c^2 - M(Z, A)c^2 = 0.63$ MeV] falls in the narrow range defined by the two most frequent transitions.

Effective masses, calculated from experimental values of nuclear level spacings by Eqs. (12) and (13), are given in Table VI. The effective mass is relatively insensitive to changes in the value of $D_0 (\delta M^*/M^* = 0.2 \delta D_0/D_0)$. Because level densities quoted here are those of a compound nucleus (excitation energy Q) formed by a neutron plus the target nucleus, the effective masses correspond to nucleus (Z, A+1) instead of (Z, A). However, the level densities do not vary strongly with A except at magic numbers. These M^*'s can be compared directly with the values from μ-meson capture for the Gaussian or excited Fermi gas momentum distributions (Tables VII and VIII). They are in reasonable agreement considering the large errors that measurements of nuclear level densities may have.

In the above discussion we have used a model that did not include the effects of direct emission of neutrons or of nucleon clustering at the nuclear surface. That these effects are important has been shown by Singer.[18,24] He has calculated the fraction of direct emission for the four heaviest elements used here and the nuclear clustering correction for silver.

The effect of neutron direct emission is to reduce the predicted $\langle n \rangle$ in these heavy elements, with an attendant reduction in the effective mass necessary to give the experimental average multiplicity (Table X). M^* decreases by $\approx 20\%$ for the Fermi-gas model, $\theta_f = 8$ MeV, and by $\approx 15\%$ for the Gaussian, $\alpha^2/2M = 20$ MeV. The direct

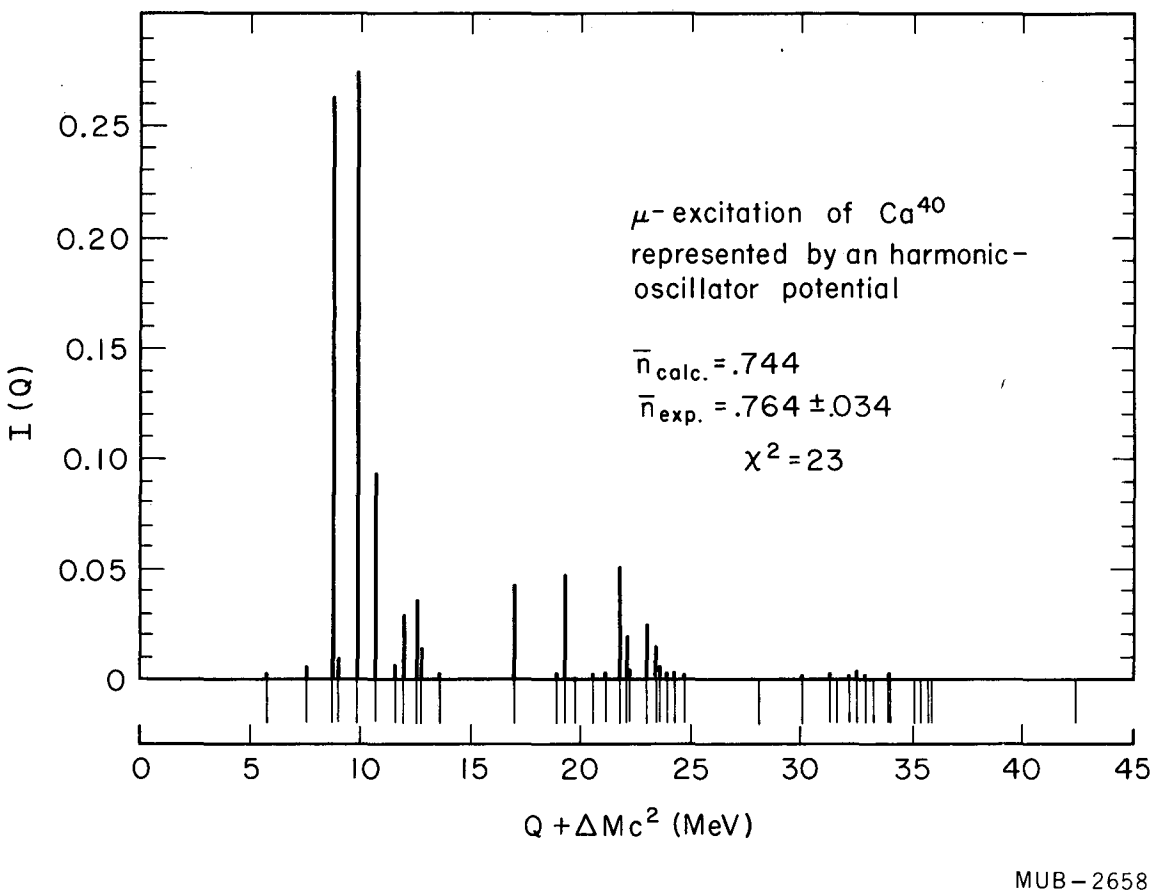

Fig. 25. μ^- excitation of Ca^{40}. Shell-model calculation, harmonic oscillator potential. $\langle n_{calc} \rangle = 0.744$; $\langle n_{exp} \rangle = 0.746 \pm 0.032$; $\chi^2 = 23$.

emission correction generally improves the fit with the multiplicity distribution for the 8-MeV Fermi gas model; for the 20-MeV Gaussian model it gives a substantial improvement in every case.

Taking into account the effect of the nuclear surface, Singer's clustering correction with the emission of two neutrons will increase the predicted $\langle n \rangle$. For silver the effect is to increase the effective mass by 10% above the value based on the direct emission correction. The multiplicity distribution for silver with the Gaussian model and with both corrections gives good agreement with the experimental values.

Table X. Gaussian distribution, $a^2/2M$ = 20 MeV; and Fermi gas distribution, θ_f = 8 MeV. Effective mass, χ^2, and predicted multiplicity distribution when Singer's direct emission and clustering corrections are made.

Target	Direct emission parameter	Clustering parameter	M^*/M	χ^2	Multiplicity distribution P_0	P_1	P_2	P_3	P_4	P_5
Gaussian, $a^2/2M$ = 20 MeV										
Ag	0.216		0.374	12.5	0.393	0.402	0.146	0.050	0.008	0.001
I	0.199		0.483	18.4	0.426	0.407	0.128	0.035	0.004	
Au	0.157		0.408	21.7	0.390	0.389	0.157	0.054	0.009	0.001
Pb	0.153		0.421	22.6	0.377	0.392	0.165	0.055	0.010	0.001
Ag	0.216	0.144	0.409	5.1	0.375	0.419	0.162	0.038	0.005	
Fermi gas, θ_f = 8 MeV										
Ag	0.216		0.275	19.2	0.400	0.385	0.156	0.052	0.007	
I	0.199		0.311	29.1	0.434	0.390	0.137	0.036	0.002	
Au	0.157		0.204	24.0	0.389	0.388	0.161	0.054	0.008	
Pb	0.153		0.178	32.3	0.387	0.374	0.170	0.058	0.010	0.001
Ag	0.216	0.144	0.305	9.9	0.381	0.405	0.171	0.039	0.004	

VI. CONCLUSIONS

The average nuclear excitation can be inferred fairly exactly from the average neutron multiplicity by means of evaporation theory. This value of $\langle Q \rangle$ is insensitive to the momentum distribution, effectibe mass, or other model parameters, the variation being no more than ± 1 MeV. When the average neutrino momentum, inferred from $\langle Q \rangle$, is expressed in units of a reduced μ mass (the rest-mass energy minus its K-shell binding energy), the result (with the exception of calcium) is constant, 0.82 ± 0.01, over the wide range of atomic numbers covered.

With the model we have taken for neutron emission from μ-meson capture the average neutron multiplicity data for most of the elements cannot be fitted with a nucleon mass within the nucleus that is equal to the unbound mass. Instead, a reduced effective mass must be assumed in order to get agreement with the average multiplicities and the related values of $\langle Q \rangle$. There is a fairly smooth decrease of this effective mass with increasing atomic number. Effective masses estimated from nuclear level densities are in fair agreement with our values. A theoretical calculation by Brueckner of the effective mass of Zr^{90} is within 10% of the values we get for silver (which is our target closest in atomic weight to Zr^{90}).

The multiplicity distributions predicted by our model are not in quantitative agreement with the experimental results (except for silicon and calcium). Inclusion of Singer's direct emission correction for the four heaviest elements uniformly improved this agreement. For silver, his additional correction for nuclear clustering reproduced the experimental distribution within statistics. However, our calculations with other elements, for reasonable values of the clustering parameter, did not lead to significant improvement.

ACKNOWLEDGMENTS

A number of people have contributed to this experiment. Principal among these the author wishes to thank Dr. Selig N. Kaplan and Dr. Robert V. Pyle for their continuing help and encouragement as well as collaboration in the experiment.

The author wishes to thank Professor Burton J. Moyer for his supervision and support of this research.

Thanks are due to Miss Betty Blaine and Mr. Robert Brians for reading a great amount of film, and to Dr. Justo A. Diaz for help during the experimental work. We have had several helpful discussions with Dr. Hans Mang.

This work was performed under the auspices of the U. S. Atomic Energy Commission.

APPENDIX

A. Background Subtraction

Background-Subtracted Multiplicity Distribution

If $(F_0, F_1, F_2, \cdots)$ represents the multiplicity distribution including a distribution of background $(B_0, B_1, \cdots)$, and if $(P_0, P_1, \cdots)$ is the distribution without background, then

$$F_n = \sum_{k=0}^{n} B_{n-k} P_k . \tag{14}$$

This can be solved for the P's,

$$P_k = \sum_{n=0}^{k} A_{k-n} F_n, \tag{15}$$

where $(A_0, A_1, \cdots)$ are functions of the B's. If the background is a Poisson distribution with an average of β pulses per sweep, i.e.,

$$B_n = \exp(-\beta) \frac{\beta^n}{n!} , \tag{16}$$

then the A's are given by

$$A_n = \exp(\beta) \frac{(-\beta)^n}{n!} . \tag{17}$$

The background-subtracted average multiplicity is given by

$$\langle n \rangle_P = \langle n \rangle_F - \beta,$$

where the average multiplicities are defined in the usual way:

$$\langle n \rangle_F = \sum_{n=0} n F_n \Big/ \sum_{n=0} F_n = \sum_{n=0} n F_n, \text{ etc.}$$

B. Statistical Errors from Background Subtraction

Derived below is the covariant matrix ("error" matrix) that is associated with the background-subtracted multiplicity distribution (P_0, P_1, P_2, $\cdots$) for a given run of N events where the average (Poisson) background was β.

The statistical fluctuations in the P's are due to two causes:

a. The statistical fluctuations in the multiplicity distribution of the real-plus-background pulses, (F_0, F_1, $\cdots$), because of a run of only a finite number N of events.

b. The variation of the instantaneous background rate because of variations of beam level during this run of N events.

These two sources of variations in the P's are statistically independent.

Let P_k be the "true" value of P_k' be the value of P_k obtained in one of a large number of repetitions of a run of N events. Then $\delta P_k = P_k' - P_k$ is the error in P_k for this particular repetition of the run. If hexagonal brackets about a quantity represent the average of that quantity over this large number of repetitions, then this average error is zero; $\langle \delta P_k \rangle = 0$, since $\langle P_k' \rangle = \langle P_k \rangle = P_k$, by definition. However, $\langle \delta P_k \, \delta P_\ell \rangle$ is not zero in general. From Eq. (15) we get

$$\delta P_k = \sum_{n=0}^{k} \left[A_{k-n} \, \delta F_n + F_n \, \delta A_{k-n} \right].$$

(We are neglecting a term proportional to $\delta F_n \, \delta A_{k-n}$ which turns out to be small). The covariant matrix is

$$\langle \delta P_k \, \delta P_\ell \rangle = \sum_{m=0}^{k} \sum_{n=0}^{\ell} \Big[\langle A_{k-m} A_{\ell-n} \rangle \langle \delta F_m \, \delta F_n \rangle + \langle F_m F_n \rangle \langle \delta A_{k-m} \, \delta A_{\ell-n} \rangle$$

$$+ \langle A_{k-m} \, \delta A_{\ell-n} \rangle \langle F_n \, \delta F_m \rangle + \langle A_{\ell-n} \, \delta A_{k-m} \rangle \langle F_m \, \delta F_n \rangle \Big].$$

The last two terms are zero if we assume that

$$\langle F_n \delta F_m \rangle = \langle F_n \rangle \langle \delta F_m \rangle, \text{ since } \langle \delta F_m \rangle = 0.$$

The quantity $\langle \delta F_n \, \delta F_m \rangle$ is the binomial covariant matrix

$$\langle \delta F_n \delta F_m \rangle = F_n (1 - F_n)/ N \qquad \text{for } n = m$$

$$= - F_n F_m / N \qquad \text{for } n \neq m.$$

This matrix is nondiagonal, since the components of $(F_0, F_1, \cdots)$ are normalized to 1 and therefore not independent.

A variation in A_{k-m} is due to a variation in the average background rate, β (Eq. 17):

$$\delta A_{k-m} = \frac{\partial A_{k-m}}{\partial \beta} \delta\beta \equiv a_{k-m} \delta\beta$$

and

$$\langle \delta A_{k-m} A_{\ell-n} \rangle = a_{k-m} a_{\ell-n} \langle \delta\beta^2 \rangle \equiv a_{k-m} a_{\ell-n} \sigma^2.$$

The covariant matrix then becomes after substitution (for $k < \ell$),

$$\langle \delta P_k \delta P_\ell \rangle = \left[\sum_{m=0}^{k} (A_{k-m} F_m A_{\ell-m}) - P_k P_\ell \right] \cdot \frac{1}{N} + G(k) G(\ell) \sigma^2,$$

where

$$G(k) = \sum_{m=0}^{k} F_m a_{k-m} .$$

For simplicity, the errors quoted in the experimental multiplicity distributions derive from ignoring the off-diagonal terms in the covariant matrix for the P's so that, if $P_k' = P_k \pm \Delta P_k$, then ΔP_k was assumed to be

$$\Delta P_k = \left[\langle \delta P_k \delta P_k \rangle \right]^{1/2} .$$

REFERENCES

1. V. L. Fitch and J. Rainwater, Phys. Rev. 92, 789 (1953); D. L. Hill and K. W. Ford, Phys. Rev. 94, 1617 (1954); L. N. Cooper and E. M. Henley, Phys. Rev. 92, 801 (1953); J. C. Sens, CERN 63-29, p. 143 (1963).
2. J. S. Baijal, J. A. Diaz, S. N. Kaplan, and R. V. Pyle, Nuovo Cimento 30, 711 (1963).
3. J. A. Diaz, S. N. Kaplan, and R. V. Pyle, Nucl. Phys. 40, 54 (1963).
4. Donald E. Hagge, Neutron Energy Spectra from Nuclei Excited by μ^--meson Capture (Ph. D. Thesis), Lawrence Radiation Laboratory Report UCRL-10516, June 1963 (unpublished).
5. S. N. Kaplan, B. J. Moyer, and R. V. Pyle, Phys. Rev. 112, 968 (1958).
6. E. Fermi and E. Teller, Phys. Rev. 72, 399 (1947); R. Huby, Phil. Mag. 40, 685 (1949); W. F. Fry and G. R. White, Phys. Rev. 93, 1427 (1954).
7. R. M. Tennant, The Absorption and Decay of Negative Pions, in Progress of Elementary Particle and Cosmic Ray Physics, Vol. V, J. G. Wilson and S. A. Wouthuysen, Eds. (North-Holland Publishing Company, Amsterdam, 1960), p. 367.
8. H. Morinaga and W. F. Fry, Nuovo Cimento 10, 308 (1953).
9. M. N. Rosenbluth, Phys. Rev. 75, 532 (1949).
10. J. Tiomno and J. A. Wheeler, Rev. Mod. Phys. 21, 153 (1949).
11. M. F. Crouch and R. D. Sard, Phys. Rev. 85, 120 (1952); A. M. Conforto and R. D. Sard, Phys. Rev. 86, 465 (1952). M. Widgoff, Phys. Rev. 90, 892 (1953); S. N. Kaplan, B. J. Moyer, and R. V. Pyle, Phys. Rev. 112, 968 (1958); L. Winsberg, Phys. Rev. 95, 205 (1954); G. Groetzinger, M. J. Berger, and G. W. McClure, Phys. Rev. 81, 969 (1951); D. R. Jones, Phys. Rev. 105, 1591 (1957).

12. J. M. B. Lang, Proc. Phys. Soc. (London) A65, 995 (1952).
13. T. B. Taylor, Phys. Rev. 92, 831 (1953).
14. P. J. Wyatt, J. G. Wills, and A. E. S. Green, Phys. Rev. 119, 1031 (1959).
15. M. H. Johnson and E. Teller, Phys. Rev. 98, 783 (1955).
16. K. A. Brueckner and J. L. Gammell, Phys. Rev. 109, 1029 (1958).
17. K. A. Brueckner, A. M. Lockett, and M. Rotenberg, Phys. Rev. 121, 255 (1961).
18. P. Singer, Nuovo Cimento 23, 669 (1962).
19. J. B. Cladis, W. N. Hess, and B. J. Moyer, Phys. Rev. 87, 425 (1952).
20. J. M. Wilcox and B. J. Moyer, Phys. Rev. 99, 875 (1955).
21. L. S. Azhgirey, I. K. Vzorov, V. P. Zrelov, M. G. Mesheryakov, B. S. Neganov, R. M. Ryndin and A. F. Shabudin, Nucl. Phys. 13, 258 (1959).
22. E. Henley, Phys. Rev. 85, 204 (1952).
23. Selig N. Kaplan (Lawrence Radiation Laboratory), private communication, 1964.
24. P. Singer, Phys. Rev. 124, 1602 (1961).
25. E. Clementel and C. Villi, Nuovo Cimento 9, 950 (1958).
26. J. R. Luyten, H. P. C. Rood, and H. A. Tolhoek, Nucl. Phys. 41, 236 (1963).
27. Sven Gösta Nilsson, Kgl. Danske Videnskab. Selskab Mat.-Fys. Medd. 29, No. 16 (1955).
28. K. J. LeCouteur, The Statistical Model, in Nuclear Reactions, Vol. 1, P. M. Endt and M. Demeur, Eds. (North-Holland Publishing Company, New York, 1959), p. 318.
29. E. R. Graves and L. Rosen, Phys. Rev. 89, 343 (1953).
30. M. A. Preston, Physics of the Nucleus (Addison-Wesley Publishing Company, Inc., Reading, Massachusetts, 1962) p. 192.
31. L. G. Gomes, J. D. Walecka, and V. F. Weisskopf, Ann. Phys. (N. Y.) 3, 241 (1958).

32. F. Bjorklund and S. Fernbach, Phys. Rev. 109, 1295 (1958); and F. Bjorklund in Proceedings of the International Conference on the Nuclear Optical Model, Tallahassee. The Florida State University Studies (Tallahassee, 1959) No. 32.

33. J. H. Coon, R. W. Davis, H. E. Felthauser, and D. B. Nicodemus, Phys. Rev. 111, 250 (1958).

34. S. Rand, Phys. Rev. 107, 208 (1957).

35. This method of reducing the relative number of π's is due to N. Campbell and Robert A. Swanson (University of Chicago), 1958 (unpublished).

36. The tank used here is the one used and described by Hicks, Ise, and Pyle (reference 38) and S. N. Kaplan et al. (reference 5).

37. Donald A. Hicks, John Ise, Jr., and Robert V. Pyle, Phys. Rev. 101, 1016 (1956).

38. B. C. Diven, H. C. Martin, R. F. Taschek, and J. Terrell, Phys. Rev. 101, 1012 (1956).

39. A. B. Smith, P. R. Fields, and J. H. Roberts, Phys. Rev. 108, 411 (1957).

40. E. I. Dolinsky and L. D. Blokhintsev, Nucl. Phys. 10, 527 (1959).

41. Elihu Lubkin, Ann. Phys. (N.Y.) 11, 414 (1960).

42. Richard R. Silbar, Nilsson Model Calculations of Mu Capture Rates in 2s - 1d Nuclei (Ph. D. Thesis), University of Michigan, Ann Arbor, Michigan, 1963.

43. Gladys H. Fuller, Relative Isotopic Abundances, in 1959 Nuclear Data Tables, K. Way, Ed. (U. S. Government Printing Office, Washington 25, D. C., 1959) p. 66. Abundances not quoted in our table were neglected. The sum of those quoted for an element were normalized to unity in our calculations.

44. L. A. König, J. H. E. Mattauch, and A. H. Wapstra, Nucl. Phys. 31, 18 (1962).

45. Kenneth W. Ford and John G. Wills, Calculated Properties of Mu-Mesonic Atoms, Los Alamos Scientific Laboratory Report LAMS-2387, Nov. 1959.

46. Al, Si, Ca: J. C. Sens, Phys. Rev. 113, 679 (1959); Fe, Ag, Au, Pb: S. N. Kaplan, J. S. Baijal, J. A. Diaz, G. Kojoian, and R. V. Pyle, Lifetimes in Medium and High- Z Elements, Lawrence Radiation Laboratory Report UCRL-10297, June 1962 (unpublished); Iodine: T. A. Filipas, R. Palit, R. T. Siegel, and R. E. Welsh, Negative Muon Capture Rates in High-Z Elements, Carnegie Institute of Technology Report NYO-10563, July 1963 (unpublished).

47. R. W. Huff, Ann. Phys. (N.Y.) 16, 288 (1961).

This report was prepared as an account of Government sponsored work. Neither the United States, nor the Commission, nor any person acting on behalf of the Commission:

A. Makes any warranty or representation, expressed or implied, with respect to the accuracy, completeness, or usefulness of the information contained in this report, or that the use of any information, apparatus, method, or process disclosed in this report may not infringe privately owned rights; or

B. Assumes any liabilities with respect to the use of, or for damages resulting from the use of any information, apparatus, method, or process disclosed in this report.

As used in the above, "person acting on behalf of the Commission" includes any employee or contractor of the Commission, or employee of such contractor, to the extent that such employee or contractor of the Commission, or employee of such contractor prepares, disseminates, or provides access to, any information pursuant to his employment or contract with the Commission, or his employment with such contractor.